North America Dynamics and Western U.S. Tectonics

Eugene D. Humphreys and David D. Coblentz[1]
Department of Geological Sciences, University of Oregon, Eugene, Oregon, USA
[1]Now at Las Alamos National Lab, New Mexico, USA

Interest and controversy exists on the origin of forces that move and tectonically deform plates, especially regarding the relative importance of loads applied to the plate margins, base and those created internally, such as by high elevations. To quantify these loads, we predict the observed stress field by applying loads to a 2D North America plate model, finding that boundary loads are most important, followed by internal and basal loads. Craton-root basal drag of ~4MPa opposes absolute plate motion, compared to basal tractions elsewhere that average ~0.4MPa, suggesting that North America is separated from a relatively static deep Earth mantle by a weak asthenosphere. San Andreas shear (~1.5TN/m), gravitational collapse and southern Cascadia pull all contribute importantly to western U.S. deformation; the region also is relatively weak. Important future work includes incorporating 3D plate structure onto global flow calculations and including the global set of plates.

1. Introduction

The tectonic motion and deformation of a plate are responses to the forces acting on it. The classical view of the forces responsible for plate motion has edge forces driving rigid plates over a weak and relatively static asthenosphere that acts to resist plate motion. Recently, this view has been challenged by some global geodynamicists, who advocate a model with mantle flow (driven primarily by ocean lithosphere sinking in the lower mantle) driving plates from below. The forces driving plate motion also generate tectonic stresses responsible for earthquakes and lithospheric deformation. A point of particular significance and continued contention is the relative and absolute importance of loads applied to the plate margin, base, and interior. On a smaller scale, knowledge of stress magnitude on plate boundaries bears directly on fault stress levels, faulting mechanics and the distribution of stress through the crust and mantle lithosphere.

The North American plate offers good opportunity for making progress on understanding the origin and magnitude of plate forces, given the relatively simple and well-understood nature of the boundary loads acting on the plate and the abundance and large spatial distribution of observed intraplate stress indicator data. In this paper, North America stress indicators are used to evaluate the magnitudes of the various tectonic loads acting on this plate. Our modeling of plate stress is presented in an appendix. This modeling incorporates approximates for all the important tectonic loads acting on the North American plate, and the goal is to estimate the relative and absolute importance of these loads to the horizontal stresses within North America.

Fig. 1 illustrates the origin of the various loads (i.e., forces) acting on a plate, and by force balance these loads sum to zero (see also *Lithgow-Bertelloni and Guynn* [2004] for a good discussion on the basic physics of plate stresses). These loads can be grouped into categories: edge forces, basal tractions, and internal loads arising from crustal and uppermost mantle density structure. Edge forces are created directly by plate-to-plate interaction across shared plate boundaries. Stress continuity requires that two plates in contact apply equal but opposite forces on each other across the shared boundary. Stress continuity holds across any chosen surface, so that isolating the loads acting on plate boundaries can be seen as a convenient way of isolating a plate from neighboring plates. Plate density structure not only creates surface elevation through isostasy, the resulting gravitational potential energy (GPE) plays a role in creating horizontal stresses within the plate. These stresses result from the depth-integrated vertical stress created by the weight of the overburden rock [e.g., Fleitout, and Froidevaux, 1982]; the horizontal gradient of this integral through the lithosphere creates horizontal deviatoric stresses available for tectonic processes. When these stresses drive extension the processes is commonly referred to as gravitational collapse. The stress contribution created by GPE is both one of the more difficult quantities to estimate, and the one plate load that is estimated with an actual magnitude (i.e., not simply relative information). Because GPE yields absolute units, it provides the reference needed to scale the applied loads to absolute units of stress. Tractions acting on the base of a plate result from viscous flow in the Earth's interior, either that created by sub-lithospheric density structure (e.g., subducted slabs) or by plate motion with respect to the deeper Earth. Basal tractions on a plate are a result of viscous flow in the Earth's interior, either that created by sub-lithospheric density structure (e.g., subducted slabs) or by relative plate motion with respect to the deeper Earth. Basal tractions can be either vertical, giving rise to dynamic

topography, or horizontal. Each contributes importantly to horizontal stresses within a plate. The importance of vertical tractions can be understood by recognizing that the resulting dynamic topography contributes to the GPE. If the distinction between isostatic and dynamic topography is made by distinguishing between the effects of lithospheric and sub-lithospheric density structure [e.g., *Panasyuk and Hager*, 2000], then "ridge push" gravity sliding is a result of dynamic topography.

1.1 The Forces That Move Plates

The intact motion of plates away from spreading centers and toward subduction zones led early workers to conclude that plates are bounded by relatively weak boundaries and basal conditions and that gravitational forces both in the form of plates sliding away from ridges ("ridge push") and the pull of subducted slabs ("slab pull") are most important plate-driving mechanisms [e.g., *Elsasser*, 1969; *McKenzie*, 1969; *Morgan*, 1972; *Minster et al.*, 1974]. The plate velocity models that quickly followed [*Forsyth and Uyeda* 1975; *Chapple and Tullis*, 1977] found that slab pull was the most important force applied to plates, and that tractions on the base of continents slightly resist motion. More recent and physically complete Earth models support the conclusions that a weak asthenosphere results in plates that are weakly coupled to the underlying mantle [*Morgan et al.*, 1995] and in addition that weak faults bound plates [*Zhong and Gurnis,* 1996; *Zhong et al.*, 1998]. Models that include mantle flow driven by the sinking slabs (as inferred from geoid data, tomography or subduction history) conclude that subduction-related mantle flow provides the dominant driving force [*Zhong et al.*, 2000; *Lithgow-Bertelloni and Richards*, 1998; *Becker and O'Connell*, 2001; *Forte and Mitrovica*, 2001].

Within the framework of rigid plates, "slab pull" and slab-driven flow produce similar effects and are difficult to distinguish. In the former, upper mantle slab applies load near the subduction margin and lower mantle slab has little effect, whereas in the latter, flow driven by lower mantle slab can dominate plate loading [*Lithgow-Bertelloni and Richards*, 1998; *Becker and O'Connell*, 2001; *Forte and Mitrovica*, 2001] and basal tractions are distributed more widely over the base of a plate. Plate stress models have a potential to resolve the distribution of the loads applied to plates. However, earlier models [e.g., *Sykes and Sbar*, 1973*; Solomon et al.*, 1975; *Richardson et al.*, 1976] did not incorporate space-varying basal tractions that would distinguish between basal and plate margin loading. The more recent modeling of *Steinberger et al.* [2001], which incorporates global flow explicitly into the consideration of plate stress, indicates that global stress orientation data can be explained well by either model, but that stress magnitude and the details of stress orientation differ between these two models, permitting observationally based discrimination.

The location of the imaged subducted Farallon slab beneath eastern U.S. offers a clue on the nature of lower mantle flow beneath North America. *Grand et al.* [1997] and *Bunge and Grand* [2000] find that the location of subducted Farallon slab in the lower mantle beneath eastern U.S. is predicted well by models that have the Farallon slab dropping passively from the western North America paleo-subduction zone, which then is overridden by the moving North America plate. The portion of the Farallon slab thought to have been involved in the Laramide orogeny is found displaced ~1500 km east *Bunge and Grand* [2000], as predicted by flat-slab subduction during the Laramide [e.g., *Coney and Reynolds*, 1977; *Spencer*, 1996]. The ability of these simple models to account for slab location suggests that beneath North America no major drift of the lower mantle has occurred relative to a global reference.

To date, 3D modeling of the effects of global flow on plate stress has not included lateral variations in viscosity, such as that exhibited by deep craton roots. If coupling at the root is great compared to the rest of the plate, then stresses around the craton should indicate whether coupling is drive or drag in nature. *Wesnousky and Scholz* [1980] used this reasoning to argue for cratonic drag as North America moves over a relatively static mantle. *Fouch and Fisher* [2000] made a similar suggestion based on mantle anisotropy, which they interpreted to indicate asthenosphere flow deflecting around the North American craton. In contrast, *Bolkelmann* [2002a, b] used inferred anisotropic fast-axis dip derived from P-wave travel-time delays to argue that mantle flow has driven North America.

1.2 Origin Of North America Intraplate Stress Field

The causes of plate stress and resulting tectonic activity in various portions of North America is the subject of many papers. This is especially true in the western U.S., where the causes of deformation occurring broadly over much of the western U.S. have been of particular interest. *Jones et al.* [1998], *Sonder and Jones* [1999], *Flesch et al.* [2000], *Zoback and Mooney* [2003], *Lithgow-Bertelloni and Guynn* [2004] and others provide reviews and extensive citation lists on these subjects from their different points of view.

The general ENE-WSW compression of eastern Canada (see Fig. 2), U.S. and Atlantic basin has been

attributed to "ridge push" [e.g., *Zoback*, 1992; *Richardson and Reding*, 1991] and to mantle flow converging beneath the eastern seaboard above the sinking Farallon slab [e.g., *Lithgow-Bertelloni and Richards*, 1998; *Becker and O'Connell*, 2001; *Forte and Mitrovica*, 2001]. The extension common in the western U.S. has been attributed to gravitational collapse of this high-standing (high potential energy) region [*Jones et al.*, 1996; *Flesh et al.*, 2000] and to stresses caused by cratonic root drag [*Wesnousky and Scholz*, 1980]. Stress orientations in most of westernmost North America are consistent with right-lateral transform coupling with the Pacific plate [*Atwater*, 1970; *Flesch et al.*, 2000; *Liu and Bird,* 2002] and oblique subduction of the Juan de Fuca beneath Washington and Oregon [*Wang et al.*, 1997]. Important areas of compression occur within the Cordillera as well. A zone of contraction trending from NW to SE Washington accommodates the northern transport of California and Oregon [*Wang et al.,* 1997; *Wells et al.,* 1998]. Compressive stress radiating away from the easternmost Aleutian subduction zone has been explained by collision of the Yakutat block with North America [*Mazzotti and Hyndman*, 2002; *Hyndman et al*., 2005]. *Jones et al.* [2004] attribute thrust faulting in the central California Coast Ranges to a push of the Sierra Nevada block against the Pacific plate, driven by the locally large margin-normal GPE gradient there, and many authors have attributed thrusting in the southern California Transverse Ranges to lithospheric downwelling beneath these ranges [*Bird and Rosenstock*, 1984; *Humphreys and Hager*, 1990; *Houseman et al.,* 2000]. Our results support and quantify these conclusions.

2. North America Stress Observations

The 2004 release of the World Stress Map Project [*Reinecker et al.*, 2004] contains nearly 3000 indicators for the North American plate. Fig. 2 shows these indicators and the more uniformly sampled representation of stress that, in the appendix, are used for the modeling presented below. The World Stress Map data was supplemented with 19 stress estimates shown with large circles in Fig. 2a. Stress indicators are derived from various types of observations including earthquake radiation patterns, borehole measurements and volcanic alignments. These data not only have measurement errors, but they are imperfect representations of the stress field of interest to us, i.e., the time-average stress averaged over plate thickness. The issues posing the greatest concern for our modeling include: (1) most "stress indicators" are measurements of strain, which will be biased by strength anisotropy [*Zoback*, 2000; *Jackson*, 2002; 2003]; (2) actual stresses are influenced by near surface loads such as short-wavelength topography variations [*Zoback et al.,* 1989*; Zoback*, 1992], which appear to influence stress near the Colorado Plateau (Fig. 2a); (3) non-stationary stresses are associated with volcanic and earthquake cycles [*e.g., Schaff et al.,* 1998*; Rubin,* 1995], rupture terminations [*Stein et al.*, 1992] or heterogeneous slip [*Beroza and Mikumo*, 1996] and fault wiggles [*Saucier et al*., 1992]; (4) stress resulting from post-glacier rebound may [*Stein et al.*, 1979; *Bird*, 1996; *Zoback*, 2003] (or may not *Wu* [1996]) be large, which could account for the complex stress field observed in Baffin Bay and the Labrador Sea [*Hunt and Malin*, 1998] (Fig. 2a); (5) near-surface stress in coastal areas can be affected by sediment slumping or loading effects [*Nunn*, 1985], and (6) horizontal principal stress orientations may not be well constrained by strike-slip earthquakes [*Zoback*, 1992].

Despite these problems, the stress indicators define clear spatial patterns that show remarkable consistency among nearby indicators and between different types of measurement in the same area (Fig. 2), suggesting that in most areas measurement errors and locally induced stress heterogeneity do not present a serious problem in estimating the plate stress field. Furthermore, the two fields are consistent where inferred stress can be compared to young geologic strain [*Flesch et al.,* 2000].

Our estimated stress orientations and regimes (Fig. 2b) are very similar to those inferred by *Bird and Li* [1996] and *Lithgow-Bertelloni and Guynn* [2004], who averaged and smoothed earlier versions of the World Stress Map. The main difference between our sampled stress and that of these other studies is that we have chosen sample sites at specifically chosen locations, where the other studies sampled the stress at regularly spaced intervals. Where possible, our sample sites are chosen to lie in areas where consistent behavior is observed among nearby observations, and we use the method of *Coblentz and Richardson* [1996] to estimate the local state of stress by averaging nearby stress indicators. In areas of low observation density we use what data are available and keep the uncertainty of these data in mind. We do not use stress estimates from subduction zones (to avoid interface and plate bending events), near sudden transitions in tectonic style (because our model is not intended to address small-scale behavior, e.g., Cape Mendocino), from Baffin Bay and Labrador Sea (because of local stress field complexity, as discussed above), and from coastal area near the Gulf of Mexico, where sediment-loading effects [*Nunn*, 1985] are strong.

3. Loads Acting On North America

Prior studies on the origin of the North American intraplate stress field derive conclusions largely by associating an inferred load with tectonic effects in a limited area, or by using simplified models of the plate. This has resulted in a diversity of views on the importance of various boundary, basal and internal loads acting on the North American plate. To resolve the relative and absolute contributions of loads that often have similar general characteristics, we have modeled the intraplate stress field throughout the North America plate using a relatively complete set of applied loads. Our modeling loads a 2D thin spherical shell representing the North American plate with 30 boundary, basal and internal loads and solves for the magnitude of these loads. Details of the modeling are presented in the Appendix. Below we summarized these results in the context of other studies. The model that best predicts the observed stress is shown in Fig. A6 and is represented in Fig. 3. All of our successful models are similar to this best fitting model.

3.1 North America Dynamics

Our modeling suggests that North America is strongly coupled to Earth's interior only at the cratonic root, and the NE direction of root drag implies that mantle beneath North America moves at a relatively low speed compared to the SW motion of North America. We find that mantle flow driven by lower-mantle density structure creates tractions acting on the base of North America that provide an important contribution to the North America intraplate stress field, but at an estimated value of only ~20% that inferred by *Becker and O'Connell* [2000]. These tractions are less important than either stresses resulting directly from plate interaction or stresses arising from lithospheric GPE structure. In particular, we find the GPE associated with ridge push is the single most important load acting on the North American plate. This is a consequence not only of the relatively low value of basal tractions, but because ocean ridges bound the eastern and northern perimeter of the North American plate, the Mid-Atlantic Ridge is unusually high in GPE (Fig. 4), and subduction zones bound a relatively small fraction of the North American plate. Most boundary loads compress North America, whereas most subduction zones and the high GPE of the Cordillera act to create tension in much of the western plate.

We also conclude that buoyant asthenosphere beneath the North Atlantic basin is responsible not only for elevating the seafloor [e.g., *Ito et al*., 2003], but for creating more GPE than is represented in Fig. 4 (see Fig. A3 at long wavelength). This is a consequence of the buoyant mantle extending to a greater depth of compensation than assumed when constructing Fig. 4., which is reflected in the distinctive North Atlantic geoid high [*King*, 2006] shown in Fig. A4a. The buoyant mantle, being largely confined by craton roots surrounding most of the region, results in what is essentially an isostatic uplift of the ocean floor creating a geoid high, and it pushes on the craton roots, thereby pushing North America to the west.

We estimate shear tractions acting along the western North American plate transform margin to be 1.5±1.0 TN/m, and to correlate positively with the level of normal stress (Table A4), as expected for frictional behavior. By assuming that frictional strength increases linearly to a depth of 18 km, we obtain an effective friction coefficient for transform faults of 0.1-0.3. This effective friction coefficient would be half these values if we assume half of the plate-margin shear load is held by viscous deformation processes below 18 km while all normal stress is maintained above 18 km. This is not an unreasonable assumption since strain rate normal to a transform fault is negligible. Our range of estimated effective friction coefficient is similar to that found by *Bird and Kong* [1994] and *Townend and Zoback* [2000]. Fig. 5 illustrates that our resolved shear stress on the San Andreas transform margin (area of gray box), when applied to standard strength profile representations of the lithosphere (dashed lines) [e.g., *Kohlstedt et al*., 1995] results in San Andreas Fault stresses of ~40 MPa at 18 km depth, compared to values of ~100 MPa if the mantle were relatively weak (solid line) [e.g., *Jackson*, 2002]. These values compare to the ~300 MPa that would result from a friction coefficient of 0.6. Although our estimated San Andreas fault strength is "weak" in a rock mechanics sense, it is found to hold much more shear stress than the ~3 MPa released in typical earthquakes (Fig. 5, small rectangle) [*Kanamori*, 1994]. From this we conclude that either fault slip during an earthquake stops while significant shear stress remains resolved on the fault surface, suggesting that fault weakening during an earthquake is a short-lived and transient process, or shear stress approaches zero during the earthquake, such as may occur within a narrow propagating slip-pulse dislocation [*Heaton*, 1990; *Zheng and Rice*, 1998].

3.2 Western U.S. Tectonics

The forces responsible for western U.S. tectonic deformation have been addressed qualitatively since 1970 [*Atwater*, 1970] by hundreds of papers, and increasingly quantitatively through a series of papers (*Sonder et al.* [1987]; *Richardson and Reding* [1991]; *Jones et al.* [1996]; *Liu* [2001]; *Bird* [1998]; *Flesch et al.* [2000], *Lithgow-Bertelloni and Guynn* [2004]; and many studies on a more local scale). The quantitative models either have held an eastern margin fixed (without regard to the stresses that result there) or when modeling the entire plate, have done so without a sufficiently complete or resolved description of the loads to draw conclusions on a portion of plate as small as the western U.S. Our modeling is an attempt to put the western U.S. in a plate-scale context and incorporate basal tractions, a carefully constructed GPE field, and a relatively complete set of boundary loads. However, our models are limited in resolution by problems associated with being 2D, uniform in strength and having a rather simple description of the loads. Furthermore, as indicated by Fig. A7, significant parameter tradeoffs are possible for some of the western U.S. boundary loads. Nonetheless, our model accounts relatively well for the observed stresses in the western U.S. (Figs. 6, A6) and all successful models are similar to that shown in Figs. 6 and 6A. Hence, as a model of the western U.S., resolution is thought to be sufficient to address the region in general terms. The following is an assessment of our models.

Of the loads acting to deform the western U.S., two of these – transform interaction between the Pacific and North American plates and high GPE of the Cordillera – have long been recognized as important. We also recognize as important the influences of loads applied normal to the western margin of North America and tractions applied to the base of North America. A discussion of each of these loads follows.

3.2.1 Transform interaction

Transform faulting can only resist plate motion. Hence the forces responsible for relative motion must be transmitted through the plates and the occurrence of plate boundary strain concentration requires a local reduction of effective strength [*Bercovici*, 1995; 2003]. Pacific-North America transform accommodation occurs in the westernmost swath of continent. The importance of Pacific-North America transform interaction is evidenced by the shear stress indicators (Fig. 2), a common occurrence of margin-parallel right-lateral faults (Fig. 6a) distributed from coastal California east into central Nevada (including the San Andreas fault and the Eastern California Shear Zone–Walker Lane Belt), and the right-lateral shear strain seen geodetically over the same area [*Bennett et al.*, 1999; *Thatcher*, 2003]. This regional influence was recognized early by *Atwater* [1970] and its role in western U.S. tectonics remains appreciated [e.g., *Flesch et al.*, 2000]. Our stress modeling suggests that 1.5±0.4 TN/m of shear stress is applied to this margin in California (Fig. 3), creating some of the greatest levels of stress to be found in western U.S. (Fig. 6). The applied transform shear load is primarily responsible for the NNW transport of the Sierra Nevada block [*Whitehouse et al.,* 2005*; McCaffrey*, 2005] and the shear stress and strain distributed across the western Great Basin (Fig. 6a). The fact that the stress and strain shear fields do not extend farther east than about central Nevada [*Bennett et al.*, 2003; *Hammond and Thatcher*, 2004] implies that the shear forces acting on the western margin of North America are balanced by forces acting on the north or south ends of the region experiencing large shear stress, as might be expected for a finite-length transform fault system [*Sonder et al.*, 1986]. Figure 6a shows that it is north-south compression across southern British Columbia and Washington (associated there with a zone of tectonic contraction [e.g*., Reidel et al.*, 1989; *Lewis et al.*, 2003]) that is primarily responsible for maintaining force balance by pushing back on the northern Great Basin and Sierra Nevada block. Figure 2b shows that in the far field, this compression is balanced by northernmost Atlantic ridge push.

It is worth noting that the zone where shear load is applied to the margin of North America continues north beyond the San Andreas fault along the length of oblique subduction, and that shear stress levels there are similar to (or greater than) those applied to the San Andreas margin (Fig. 3). The zone of oblique convergence extends north to northern Washington, where subduction geometry changes (Fig. 6) and convergence becomes approximately normal along Vancouver Island. The combination of applied shear load south of Vancouver Island and an absence of applied shear along Vancouver Island creates a dynamic buttressing effect against which the shear-entrained western U.S. jams [*Wang et al.*, 1997; *Wells et al.,* 1998, *Lewis et al.,* 2003].

3.2.2 Gravitational Potential Energy

GPE variations created by density structure within the western U.S. crust and uppermost mantle provides an important stress field that tends to drive extension [*Jones et al.*, 1996; *Flesch et al.*, 2000; *Liu*, 2001; *Thatcher*, 2003]. The abundance of western U.S. GPE and the associated extension is a classic example of crustal thickening during the Sevier and Laramide orogenies followed by post-orogenic "collapse" [*Coney and Harms*, 1984; *Livaccari*, 1991; *Burchfiel et al.*, 1992]. However, current western U.S. crust is not anomalously thick, and the high elevations and GPE are more attributable to increases in mantle buoyancy

resulting from Laramide and post-Laramide modifications in North America lithosphere [*Liu and Shen*, 1998; *Humphreys et al.,* 2003], the post-Laramide falling away of the Farallon slab [*Gurnis*, 1992], and the recent local [*Sleep*, 1990; *Saltzer and Humphreys*, 1997] to regional [*Parsons et al.,* 1994; *Lowry et al*., 2000] influence of the Yellowstone hotspot. GPE is increased where high elevations are supported by these relatively deep sources of buoyancy.

By separating the GPE-derived modeled stresses from those created by loading the plate margins and base (Fig. 6b and c), we see that GPE-derived stress contributes most importantly to driving extensional orogenic collapse of the western U.S. interior (Fig. 6c shows that no significant extension would occur without the stress resulting from GPE) and to compressing the low-lying regions in coastal California, much of Washington and the Great Plains. Our best estimate of western U.S. GPE over the Rocky Mountains and the Basin and Range (Fig. 6) is greater than that of our reference ridge, attaining greatest values near the Yellowstone hotspot. Tectonically important deformation penetrates farthest into the continent near Yellowstone (Fig. 6). The combination of extension in the area east of the Sierra Nevada block and contraction in the central California Coast Ranges to the west is a reflection of the large margin-normal GPE gradient that acts across this block (Fig. 6b) [*Eaton*, 1932; *Jones et al*., 2004].

3.2.3 Plate normal loads

The applied normal load along the western North America margin varies greatly (Fig. 3), and exerts an important influence on western U.S. tectonics. Plate-normal loading in the Gulf of California is slightly tensional (relative to our reference ridge), consistent with the trans-tensional character of this ridge-transform province. Along the San Andreas transform margin, plate-normal stresses of 0.5-1 TN/m are required to balance the push of the Sierra Nevada block against the Pacific plate (*Jones et al*. [2003] and Figs. 2 and 6c), and in our modeling we find that most of the margin of western U.S. and Canada is compressed more strongly than by our reference ridge. This tectonic state tends to hold these regions from extending. An important exception to this is the southern portion of the Cascadia subduction zone, where strong tension of about 4 TN/m (relative to our reference ridge) acts on the southern Cascadia subduction zone. This estimate is similar to the ~3 TN/m of tension found by *Govers and Meijer* [2001]. The regional effect of this tensional margin can be recognized by the focusing of tensile stress trajectories at southern Cascadia (Fig. 6a), and this local tectonic "free face" [e.g., *Mann*, 1997] provides a lack of confinement that enables the shear-entrained portion of western U.S. to move north and the Basin and Range (including the Yellowstone area) to expand [*Wells et al*., 1998]. From a kinematic perspective, the San Andreas and Queen Charlotte faults along the Pacific plate confine North America by not moving away from the continent at a significant rate, whereas southern Cascadia roll-back creates the space needed for both Great Basin dilation and Sierra Nevada translation. Thus it appears from both kinematic and dynamic considerations that the geodynamics of the southern Cascadia region is critically important for explaining a majority of the observed deformation distributed across the western U.S. interior. Specifically, it is the roll-back of southern Cascadia that facilitates western U.S. deformation. In contrast, modeled north Cascadia is compressional relative to our reference ridge, which is consistent with north Cascadia subduction tectonics [*Brandon et al.,* 1998; *Geist*, 1996] and the non-extending and nearly magmatically inactive north Cascade volcanic arc [*Sherrod and Smith*, 1990; *Wells et al*., 1998]. Such compressive subduction is anomalous for the North America subduction zones (Fig. 3).

3.2.4 Basal Tractions

We model two basal traction fields that bear on western U.S. tectonics. The effects of global flow (i.e., the field shown in Fig. A4c), as modeled, create shear stress in western U.S. lithosphere of 0-0.3 TN/m that is oriented similar to the stress field created by the San Andreas parallel load (Fig. A2c). These stresses, although not dominant, are significant relative to the other stress contributions (Fig. 6). The other modeled basal traction is that resulting from cratonic root drag. The effect of this contribution to western U.S. stress is similar in form but opposite in sign (i.e., with a NE-SW tension axis) to that created by global flow, and it is larger in magnitude, creating 0.5-0.8 TN/m of stress in the western U.S. The combined effect of the modeled basal tractions is to create 0.3- 0.5 TN/m of SW-NE tension and similar amounts of NW-SE compression. With respect to the net stress shown in Fig. 6, these stresses are most important in creating and orienting the extensional environment in the Rocky Mountain and eastern Great Basin region.

3.2.5 Summary Of Western U.S. Dynamics

In summary, the following are the principal features of western U.S. geodynamics: 1) the largest stresses (the shear stress in California and Nevada and N-S compression across Washington and southern British Columbia) can be seen as consequences of a finite-length transform margin (strike-slip and oblique subduction) that extends along the western U.S. as far north as Washington; 2) Margin normal loading tends to

confine western North America, with the tensional southern Cascade subduction zone being most significant and tectonically important exception; 3) The N-S compression in Washington and southern British Columbia is the continent-wide compression (see trajectories in Fig. 2b) caused by high GPE of the North Atlantic (Figs. 3 and A4a); regions to the south of Canada are less compressed because NE-oriented cratonic root drag creates a stress-shadowing effect that tends to protect the western U.S. Figure 6 shows that the combined effect of these plate margin and basal loads (Fig. 6c) is insufficient to drive the areal dilation in the western U.S. This extension, and significant contributions to contraction along much of the periphery of elevated western U.S., are consequences of GPE gradients (Fig. 6b).

4. Discussion and Conclusions

Forward and inverse modeling involves parameterizing a problem and seeking an optimal set of parameter values. The modeler's intuition and judgment influences modeling through the choice of how to parameterize a problem (e.g., Figs A1-A4), and the choice of what constitutes an optimal or acceptable fit (e.g., as measured by least-squares misfit using the weighting function shown in Fig. A5). It should be obvious that if an important process is not parameterized, not only is it unrepresented in the model, but that the parameters used to describe other processes may be biased as they attempt to account for something otherwise unrepresented. If the character of an unrepresented process does not suggest its activity to the modeler the process may go unnoticed and unmodeled. For instance, prior plate models have included neither the effects of root interaction on plate stress nor the effects of anomalously high GPE of the North Atlantic, and we find that these omissions could lead to misinterpretations of the cause of North America stress.

We modeled North America stress to resolve the relative and absolute importance of the causes of North America plate stress and to understand the deformation that results. In this way, the various causes of plate stress can be distinguished and the magnitude and uncertainty of the different loads can be estimated. In our modeling, we have included every major load we perceived to be of importance, and through subsequent forward modeling we modified the parameterization as we saw a need for more complete description of the loads. Based on the success of our model to account for the regional aspects and many peculiarities of the observed North America stress field, combined with an exhaustive search over a diverse set of parameters, we think that we have adequately resolved the basic origin and character of North America plate intraplate stress field. However, we readily acknowledge that the presence subtle differences between observed and modeled stress suggests that the model is incomplete in some regards; we presume this incompleteness to be of minor importance. For instance, variations from the average load along the length of a modeled section (e.g., the San Andres fault) could be important locally, but probably has little far field effect. Of more concern is the tendency for observed mid-plate SHmax orientations to define a more circular pattern (around the craton) than do the modeled stresses (see Fig. A5a). It is not clear if this is a result of an unrepresented or improperly represented load or of modeling in 2D. Significant continued progress in understanding North America stress will require a more comprehensive knowledge of the stress state (particularly the oceans and continental margins) and improved modeling capabilities (including modeling in 3D, incorporating variations in strength and rheology, and modeling global flow simultaneously with lithospheric dynamics).

In the following paragraphs we consider some interesting expressions of the stress field within North America and western U.S. When considering tectonic processes, several aspects of the dynamics – while obvious when considered – should be stated explicitly. Practically speaking, significant deformation occurs where stress magnitude exceeds rock strength (a yield strength or some reference viscous strength). Whereas strength is a local property, stress is transmitted from some distance away; stress may be created by nearby GPE variations or by distant forces and transmitted through the plates. GPE and strength fields are inherited, created by prior geologic events. And, in the absence of strength variations, GPE would create a curl-free deformation field in contrast to the divergence-free deformation field created by transform deformation.

4.1 North America

Subduction zones comprise only about a quarter of the North America plate margin, and of this, only at the small Puerto Rico subduction margin is North American plate actually being subducted. This has been an asset in modeling of North America dynamics because the regional stress influence of subduction zones is less well understood than is that of spreading and transform margins. The African plate is similar to the North American plate in this respect, which helped *Coblentz and Sandiford* [1994] to constrain the modeling of African stresses. We find that most important for North America stress are the north Atlantic and Cordilleran

ridges of high GPE, which drive extension near their respective margins and compress the North America interior.

A general result of our modeling is the estimation of absolute stress within the North American plate (Figs. 6 and 6A), which is a result of combining the information in the observed stress (which has no magnitude) and the estimated GPE. Average lithospheric deviatoric stress is about 1 TN/m, which would correspond to stress levels of 20 MPa if averaged over a plate thickness of 50 km. Similarly, we have an estimate of the tractions acting on the base of North America, which is a scaled version of that estimated by *Becker and O'Connell* [2001] combined with our estimated loads on the cratonic root (root drag and a push on its western side provided by unusually buoyant North Atlantic asthenosphere). An additional basal traction would be the sum of torque-balancing tractions (discussed in the Appendix), and this traction is not resolvably different from zero. We resolve root drag acting with an effective traction that is about an order of magnitude greater than the average basal traction acting on North America. A root drag could arise from shear traction at its base (as we model it) or from normal and shear tractions acting on its sides. Either way, if the entire upper mantle were low in viscosity, the root would not couple to the interior much more strongly than the rest of the plate, and hence our results imply that upper mantle viscosity increases near the base of the cratonic root. This suggests a relatively a well-developed asthenosphere confined the upper few hundred kilometers (away from the root), similar to that suggested for the oceans by *Morgan et al.* [1995] and *Toomey et al.* [2002]. A root drag also implies a relatively static lower mantle, which is similar to an older view of plate tectonics as a top-driven system largely decoupled from a more static deep Earth across an uppermost mantle asthenosphere. Our results differ from *Bird* [1998] and *Lithgow-Bertelloni and Guynn* [2004] (both of whom modeled plate stress but did not include a root) and *Bolkelman* [2002a, b] (based on seismic anisotropy dip azimuths), and are consistent with *Zhong et al.* [1996, 1998] and many early workers (none of whom included a root) and *Wesonousky and Scholz* [1980] (who considered the stress effects of a root).

4.2 Western U.S.

Two aspects of western U.S. deformation warrant additional comment. First, in contrast to Mexico and Canada where deformation is concentrated within narrow zones between the North America and Pacific plates, deformation in the western U.S. is spatially broad and diffuse. The former is consistent with ordinary notions of plate tectonics. Such deformation does not create geological structure in large volumes of lithosphere, and its limited diversity in tectonic style limits the study of rheological behavior. In the case of the western U.S., deformation occurs at geologically significant rates of $>10^{-16}$ s^{-1} (0.3% per m.y.) across the northern Basin and Range province, extending about 1000 km east of the Pacific plate margin (Fig. 6a) [*Bennett et al.*, 2003; *Hammond and Thatcher*, 2004; 2005]. Currently 5-10% of continental area deforms at rates $>10^{-16}$ s^{-1} [*Kreemer et al.*, 2000, 2003; *Gordon*, 1998]. As a result of western U.S. tectonic and associated magmatic activity, geologic structures are being created within large volumes of lithosphere. The utilization of the western U.S. as a natural laboratory for the study of rheological behavior has been, to date, limited in scope and holds considerable potential. Second, important contributions to western U.S. stresses arise from both gravitational collapse (i.e., deformation driven by a local concentration of high GPE) and a Pacific-North America transform interaction along a long margin. The tendency for each of these processes to produce distinctive (i.e., curl-free or divergence-free) deformation fields provides an opportunity to differentiate their relative contributions and evaluate their interactions. Simple shear deformation is confined within the western half of the deforming western U.S., whereas extension dominates deformation across the more interior portions [*Shen et al.,* 1999].

Although plate stress (such as that modeled in the appendix) is nearly independent of strength variations [e.g., *Flesch et al.*, 2001], deformation rate is not. Plate strength is controlled by a depth-integrated average of lithospheric properties [*Sonder and England*, 1989], and whether average lithospheric rheology is controlled more by faulting or viscous flow, or by the crust or uppermost mantle, are open questions [e.g., *Roy and Royden,* 2000a, b; *Jackson*, 2002]. If plate strength is viscously controlled, an effective lithospheric viscosity can be estimated by taking the ratio of stress to strain rate [*Flesch et al.*, 2001]. A viscous lithosphere results in an increase in stress with increased strain rate and tends to distribute deformation broadly [*Roy and Royden,* 2000a, b]. If faulting dominates, however, then strength is more plastic like (i.e., better described with a yield-stress rheology, with no strain-rate dependence), would be anisotropic [*Zoback*, 2000; *Jackson*, 2002], and tends to cause a more block-like deformation field. When considering the causes of western U.S. deformation, we make use of observed and modeled stress, the regional strain-rate field (as understood from geologic and geodetic studies), and qualitative reasoning to address the rheology that relates

the two. In the future, rheologically realistic, quantitative 3D modeling will permit the better-reasoned and more testable description of the region's deformation that is needed to understand the processes controlling tectonic activity.

Diffuse western U.S. deformation has been attributed to unusual lithospheric weakness and to an unusual stress state, and there is evidence for both. The important control that strength variations exert on western U.S. deformation is made obvious by the clear distinction of tectonic provinces [*Lowry and Smith*, 1995], where rapid transitions in deformation rate are too abrupt to be associated with changes in the stress state. Through modeling, *Choi and Gurnis* [2003] find that weak zones trending into the western U.S. interior are important to the occurrence of deeply penetrating shear deformation. Tectonically important deformation in the western U.S. interior (Fig. 6a) is observed to occur in weak lithosphere [*Lowry and Smith*, 1995] heated by recent intense magmatic activity [e.g., *Burchfiel et al.,* 1992; *Wernicke*, 1992; *Liu*, 2001] within the Basin and Range and Rio Grande Rift [*Coney*, 1980], Yellowstone [*Christiansen and Yeats*, 1992] and the High Lava Plains of SE Oregon [*Jordan et al.*, 2004], and the magmatically productive southern Cascades [*Priest*, 1990]. However, an in intact behavior of regions that experienced intense magmatism in the past (prior to ~10 m.y. ago, e.g., the Snake River Plain [*Anders and Sleep*, 1992], the central Great Basin [*Bennett et al*., 2003; *Hammond and Thatcher*, 2004] and the Sierra Madre Occidental [e.g., *Henry and Aranda-Gomez*., 2000]) suggests that increased lithospheric strength is a long-term effect of magmatism. This could be attributed to the effects of dehydration of the lower crust or upper mantle [e.g., *Hirth and Kohlstedt*, 1996] or a mid-crustal plutonic "healing" of faults.

In addition to the effects of unusual lithospheric strength, *Jones et al*. [1996; 1998] argue that the broad field of extension is fundamentally the result of the broad region of high western U.S. GPE. This is supported by our results, where we conclude that the tensional nature of western U.S. stress is largely a result of the GPE field. Figure 6 shows that GPE creates horizontal tension across the elevated western U.S. (Fig. 6b), and that the orientation of the least compressive direction is the result of boundary forces (Fig. 6c), especially San Andreas shear and southern Cascadia pull. It is worth noting that both south Cascadia tension and the application of right-lateral shear (by Pacific-North America relative motion) create NW-oriented tension in the area south of Cascadia, whereas these two loads create tensile directions that are nearly orthogonal to one another north of British Columbia. The tendency is for extension to occur in the northern Basin and Range but not in Canada. Similarly, north Mexican gravitational collapse toward the Mid-America subduction zone is inhibited by the right-lateral Gulf of California transform system.

Beyond these general tectonic controls on western U.S. deformation, there is a rich diversity of interesting tectonic processes expressed that often show a clear interaction of small and large scales. Some of these are well understood while others represent outstanding problems to be solved.

4.2.1 The Distributed Transform System

In the continental lithosphere north of the Gulf of California, transform accommodation broadens to occupy several important faults in northernmost Baja California, southern California, and the California Borderland [e.g., *Humphreys and Weldon*, 1995]. This broadening suggests a transition from a fracture-controlled to a viscous-controlled rheology. Farther north, transform accommodation occurs on the San Andreas fault and within the more interior Eastern California Shear Zone, which trends across the Mojave Desert [*Sauber et al*., 1994] and into a tectonically active swath [*McClusky et al.*, 2001; *Miller et al*., 2001] that lies east of the non-deforming Sierra Nevada block [*Argus and Gordon*, 1991; *Dixon et al.*, 2000; *Unruh et al.*, 2003]. The Great Valley portion of this block is ophiolitic [e.g., *Dickinson et al.*, 1996] and the batholitic Sierra Nevada portion has very low heat flow [*Saltus and Lachenbruch*, 1991], each contributing to the strength of this block. Still farther north this interior shear zone follows the Walker Lane Belt across the westernmost Great Basin [*Svarc et al*., 2002a, b; *Hammond Oldow,* 2003*; and Thatcher*, 2004, 2005] and broadens as it approaches the Pacific Northwest.

4.2.2 Pacific Northwest

In the Pacific Northwest, the San Andreas fault terminates at the Mendocino triple junction and the interior shear system is accommodated largely by the rotation of a nearly non-deforming block [*MacCaffrey*, 2005; *Svarc et al*., 2002a, b]. This block, whose western end is called Siletzia (Fig. 6), is a fragment of ocean lithosphere accreted to North America ~45 Ma [*Duncan*, 1982], and it appears to be strong. The zone of shear deformation broadens as it approaches this block across the southern Oregon and NW Nevada Basin and Range, and a wide region of N-S contraction occurs along the northern margin of the block (Yakima fold and thrust belt and the Seattle-area faults). Kinematically, block rotation and the associated deformation north and south of the block serves to focus deformation into to a narrow zone as the interior shear system trends north

to Canada. Many loads work in concert to rotate this block, including the GPE gradient (Fig. 6b), the northerly push of the Sierra Nevada block on southern Siletzia, and the set of loads acting on the Cascadia margin (north-directed shear, and west-directed pull and east-directed push on the respective south and north margin). The relative importance of these loads is not well understood at present. *Crossen and Owens* [1987] attribute the plate-normal push on northern Washington to the unusual concave-out subduction-zone geometry (related shallow dip of the subducted Juan de Fuca plate and an increased subduction zone interface coupling). In contrast, the pull on the southern Cascadia margin of North America may be attributed to the deep extent of the Gorda slab, which unlike the Juan de Fuca to the north [*Rasmussen and Humphreys*, 1988; *Bostock and Vandecar*, 1995], is imaged extending well below ~200 km [*Rasmussen and Humphreys*, 1988; *Harris et al.*, 1991]. This deep slab may provide the negative buoyancy required for this part of the subduction zone to roll back and retreat from the continent.

4.2.3 Small-Scale Convection

Upper mantle seismic tomography has found evidence for small-scale convection occurring at the base of the lithosphere beneath the southern Sierra Nevada and the southern California Transverse Ranges (respectively attributed to the sinking of the mafic roots to plutons [*Ducea and Saleeby*, 1996] and to abandoned ocean slab [*Humphreys*, 1995] or thermal lithosphere [*Houseman et al.*, 2000]). This convection has been used to explain contraction in the Transverse Ranges [*Bird and Rosenstock*, 1985; *Humphreys and Hager*, 1990] and the California Coast Ranges [*Jones et al.*, 2004]. Similarly, the sinking of thermal lithosphere is proposed beneath the eastern margin of the Rio Grande Rift [*Gao et al.*, 2004] and the buoyant ascent of partially molten mantle is proposed beneath the eastern Snake River Plain [*Saltzer and Humphreys*, 1997]. We do not model the effects of horizontal tractions created by such convection, and the stress field local to these areas may not be modeled well. For instance, our modeling does not reproduce the compressive character of the Transverse Ranges (Fig A6).

Similar convection occurring beneath other portions of the western U.S. may be discovered by the EarthScope USArray deployment, which will achieve resolution of upper mantle seismic structure at a level similar to that of the above-mentioned studies. Such small-scale convection would heat and lift the plate, and therefore contribute to evolving the plate GPE.

4.2.4 Geologic History

We are likely to view current tectonic conditions of the western U.S. as too special if we do not place the region in its greater geologic context. The western U.S. is one of Earth's great orogenic plateaus, created during the Sevier-Laramide orogeny by subduction processes [*Burchfiel et al.*, 1992; *Livaccari*, 1991]. The high-standing western U.S. is thought to be the area where flat-slab subduction placed the Farallon slab in contact with North America as far west as Colorado during the Laramide orogeny [e.g., *Coney and Reynolds*, 1977; *Humphreys et al.*, 2003]. Following this phase of contractional mountain building, yet still the Farallon plate was subducting, the region simultaneously experienced significant extension and the intense mid-Tertiary magmatism [*Coney*, 1980; *Coney and Harms*, 1984]. At any location, extension and magmatism are closely related, and over the duration ~45-20 Ma magmatic-extensional activity propagated across the Mexican and western U.S. Basin and Range province [*Armstrong and Ward*, 1991; *Christiansen and Yeats*, 1992]. Most of the area that extended following the Laramide orogeny is now nearly inactive, but the Basin and Range continues to enlarge to the NE as the Yellowstone hotspot propagates NE across the region [*Gripp and Gordon*, 2002].

During the last ~28 m.y. a right-lateral transform margin progressively replaced the subduction margin [*Atwater*, 1970] so that currently most of western North America is placed against the Pacific plate along the Gulf of California-San Andreas-Queen Charlotte transform system. Only the relatively small Cascadia subduction zone is all that remains of the subduction margin. During this duration, extensional deformation slowed and transform-related shear strain progressively increased in importance [*Wernickie and Snow*, 1998]. A relatively abrupt change to more transform-like (and less extensional) deformation occurred ~8 Ma, associated with a change in Pacific-North America relative motion [*Atwater and Stock*, 1998] (which resulted in a diminished rate of Pacific plate divergence from North America). Throughout, western U.S. extended largely by expanding over the subduction zone on its western margin; as the subduction margin diminished in size and propagated north, extension rate slowed and extension direction rotated toward the subduction zone [*Zoback and Thompson*, 1987].

5. Concluding Remarks

Current modeling is limited both by the simplifications used in its description and by weaknesses in the observations used in the modeling. One important limitation is the spatially averaged nature of model results, both laterally and in depth. Processes occurring on local scales involving variation in strength or in applied load may cause stress to deviate strongly from the average values estimated in the models of stress. Nonetheless, when considering stress in a local region, the regional stresses obtained through plate-scale modeling provides important constraint on boundary conditions and regional stress averages. An additional concern is the uncertainty in the actual gravitational potential energy field, especially in the North Atlantic. We have concluded that relatively deep buoyancy beneath the North Atlantic creates more GPE there than is represented in Fig. 4, based on the long-wavelength geoid (Fig. A4a), elevated North Atlantic seafloor, and the success of testing this hypothesis (see section 3.1, North America Dynamics, second paragraph). However, the constraining observations do not provide much detail on the density distribution or its effects on North America loading. Another concern of importance is our poor understanding of the traction field acting on the base of North America. We have simply applied to the base a thin plate the results of a global flow model, augmented with a few hypothetical loads (such as root drag). Clearly, both the nature of the applied field and the effects of assuming a thin plate would benefit from better consideration in the future. Other significant concerns include the irregular and sometimes erratic nature of the stress data, and the potential problems of modeling stress without including variations in strength (which, for instance, neglects any stress-guiding effects of strong lithospheric blocks).

In the future, more sophisticated modeling will deal with many of the above shortcomings. Of greatest interest is the incorporation of 3D plate structure onto global flow calculations, including the global set of plates (as initiated by *Bird* [1998]), and simultaneously incorporating stress and strain rate data in the modeling [e.g., *Flesch et al*., 2000], thereby addressing lithospheric rheology (ideally, as a function of depth). The incorporation of 3D plates in global flow models may be the single most important improvement to be made, and will be important both to models of lithospheric dynamics and to models of global flow.

Appendix: Modeling North America Plate Stress

A1. Method

Our goal is to model North America observed stresses with applied boundary, basal and internal loads realistically enough to understand these loads, and yet maintain a level of simplicity that facilitates parameterized evaluation of uncertainties and the testing of specific hypotheses. Stresses are modeled using the finite element method in a thin elastic spherical shell with a triangular-element mesh defined by the geometry of the North American plate (Fig. A1), with a nodal spatial resolution varying from about 75 km in the eastern part of the plate to about 20 km in western U.S. This finite-element approach is similar to many previous studies [e.g., *Bird*, 1998; *Coblentz and Richardson*, 1996; *Lithgow-Bertelloni and Guynn*, 2004], and the node distribution is similar to that of *Liu and Bird* [2002]. The assumptions and approximations behind this approach, and the reasoning behind its use in modeling plate-scale stress, have been discussed in many papers. Good discussions can be found in *Bird and Piper* [1980] and *Lithgow-Bertelloni and Guynn* [2004].

We use a basis-function approach [*Reynolds et al*., 2002] to permit evaluating the sensitivity of predicted intraplate stress to the various combinations of loads discussed below. For each load acting on the plate, the torque-balancing basal drag is computed and a "basis" stress field is computed. The resulting set of basis stress fields can then be scaled and summed to compute a predicted stress field. Stresses predicted by a set of loads are compared with observed stresses to obtain an estimate of model goodness. Calculated stress is relative to average 3D compression (i.e., pressure) to be consistent with the observed stress [*Simpson*, 1997; *Flesch et al*., 2000]. Our forward approach to modeling exploits the linearity of the purely elastic model used in our analysis. Because it is computationally efficient, we can calculate the results from millions of hypothesized load combinations and investigate the character of the solution in the vicinity of a best-fitting model. All loads are dynamic (i.e., applied as stress) and we do not model strain rates or velocities. During modeling, the stresses resulting from gravitational potential energy are fixed at their calculated values.

The modeled loads acting on North America consist of 30 separate boundary, basal and internal loads. Each plate load represents a different portion of the boundary or base or internal contribution (Fig. A1). The choice of how and where to apply the specific loads is guided by the natural tectonic elements of North America. Although this representation is a simplification of what must be a rather complicated distribution of load acting on the North American plate, it embodies the important physics of the problem with only a small number of model parameters and relates plate loading and the plate stress field in a straightforward manner. Thus, with 30 finite element calculations we obtain 30 basis stress fields (e.g., Fig. A2). Modeling then is reduced to finding the best set of scaling coefficients for these stress fields.

Our modeling technique is subject to important qualifications. First, by using a thin plate formulation we average over depth-varying stress and ignore shear stresses acting on horizontal surfaces. Second, variations in North America plate stiffness are not modeled. We tried including variable strength to represent a block-like behavior of the Colorado Plateau and Sierra Nevada within a relatively weak western U.S. We find, however, that any reasonable description of strength as a function of position, including models of uniform strength and those with three orders of magnitude variation, yields modeled stress fields that are nearly equivalent. This is a consequence of modeling stress, in which forces applied to any area must balance (strain rate, of course, will be sensitive to strength). The insensitivity of stress to variation in mechanical parameters has been noted before [e.g., *Flesch et al.,* 2001]. We avoid the ambiguity inherent with the more complicated models by using the simplest (i.e., uniform strength) model. Third, by using an elastic constitutive relation between stress and strain, we approximate a rheologically complex lithosphere with a simple representation. The difference between elastic and Newtonian viscous is trivial and diminishes altogether when Poisson's ratio is 0.5. Except in regions of very high stress gradients, the effects of a power law viscous rheology usually are not very significant (their effects essentially being equivalent to strength variations). The more serious concern is that we ignore plastic-like behavior such as may typify major fault zones.

A2. Tectonic Loads

The 30 basis stress fields we calculate can be thought of as 31 basis fields from which one has been mathematically eliminated by using the constraint that the sum of the basis loads result in no plate torque. Because each basis stress field is calculated by balancing the load's torque with a basal drag, the sum of all load-

balancing drag fields is the basal drag that balances the sum of the 30 applied loads, and it is the eliminated basis field. This field represents the traction on the base of North America that is not modeled by the other basal traction fields discussed below.

A2.1 Interior Loads

Interior loads are created by tractions acting on the base of North America and by horizontal gradients of the gravitational potential energy of the plate.

A2.1.2 Potential Energy

The heterogeneous density distribution beneath North America contributes forces acting on its lithosphere. A common way to calculate the effect of 3D variations in density is to vertically integrate the vertical density moment (density times depth) to obtain a 2D field of gravitational potential energy per unit area $GPE(x,y)$ [e.g., *Fleitout and Froidevaux,* 1982*; Fleitout*, 1991; *Molnar and Lyon-Caen*, 1988], and then take the horizontal gradient of this field to obtain an equivelant horizontal plate traction [*Richardson and Reding*, 1991]. An alternative approach for obtaining GPE is to rescale the geoid [*Haxby and Turcotte*, 1978], which yields a $GPE(x,y)$ estimate that is essentially equivalent to integrated density moment, provided that lithosphere-scale density contributions to the geoid can be isolated from deeper contributions. This can be difficult in practice because filtering to remove longer wavelength deep-source geoid contributions also removes the contributions from long wavelength near-surface sources.

We estimate $GPE(x,y)$ using the geoid at wavelengths shorter than some crossover wavelength and integrated density moment at longer wavelengths. Density moment calculations use the crustal density model Crust 2.0 [*Bassin et al*., 2000; *Laske and Masters*, 2002], which provides a global estimate of crustal density derived from seismic data and a crust-type categorization. Crust 2.0 values are averages of crustal density and elevation over two degrees in latitude and longitude. For each point, we calculate the mantle density needed to maintain local isostasy by assuming mantle of uniformly perturbed density extends from 50–125 km depth. (Note: the normal Airy isostasy associated with topography and crustal thickness variation is inherent in Crust 2.0.) We model using GPE estimated with a set of cross-over wavelengths at 600, 1250, 2500, 4000, 5000, and 7500 km to avoid being limited by a preconceived choice. Using a 1250-km cross-over wavelength, for instance, excludes most geoid signal resulting from structure deeper than 125 km. (Using $A/A_0 = (1\text{-}z/r_e)^{l+1}$ for amplitude attenuation A/A_0, depth z, Earth radius r_e and spherical harmonic order l, geoid created by a harmonic mass of wavelength 1250 km at 125 km depth is attenuated by a factor of two). The 1250 km crossover wavelength is a convenient reference GPE field because it incorporates the portion of the geoid we can confidently associate with uppermost mantle and crustal structure, and it corresponds to our assumed depth of compensation.

However, GPE estimates are very similar for crossover wavelengths between 600 and 2500 km. Fig. A3 shows this, and makes the point that our crust-based and our geoid-based GPE estimates are very similar for wavelengths of 2500 km and shorter. This can be seen by comparing the two frames in lower left portion of this figure and noting that the geoid contributions to GPE are quite different in these two cases (the geoid contributions at wavelength of 1250 km and shorter has very little energy, whereas and the geoid contribution at wavelengths of 2500 km and shorter contributes about half the energy for the GPE estimate), whereas the total GPE estimates are very similar. Recognizing that the problems associated with each of these estimates for GPE are different (i.e., uncertainty in the density structure near the surface and deep in the Earth), the near independence of our GPE estimate on the crossover wavelength at wavelengths of 2500 km and shorter leads us to conclude that the GPE is estimated well for these wavelengths. Note that because the models using a cross-over wavelength of 600 km (which rely nearly entirely on Crust2.0) and 2500 km (which makes significant use of the geoid) produce both similar GPE estimates and estimates of model parameters (Fig. 3), we are confident our models are not strongly biased by errors in the GPE estimate for wavelengths of 2500 km and shorter.

In addition to excluding geoid created by deep structure, filtering out long wavelength geoid excludes signal created by long wavelength upper mantle structure. The excluded long wavelength geoid contains information on upper mantle density structure that may be mis-estimated in our density-moment calculations for some reason (e.g., because of an incorrectly assumed depth of compensation). Fig. A3 shows that GPE estimated with a 5000-km crossover wavelength admits relatively large amounts of long wavelength geoid. This GPE estimate contains ~25% more amplitude in the North Atlantic than do GPE estimates filtered to exclude geoid wavelengths longer than 2500 km. It also contains a prominent geoid low extending from Hudson Bay to the Caribbean subduction zone, which appears have a contribution from the lower mantle

Farallon slab [e.g., *Grand*, 1994; *Grand et al.*, 1997; *Conrad et al.*, 2004]. Hence, while the North Atlantic geoid high may contain important information on the upper mantle, the GPE estimate with this signal appears to be contaminated by significant amounts of signal from the lower mantle. The possible effects of a long-wavelength North Atlantic GPE high are dealt with independently in the North Atlantic Craton Push section below.

Mid-Ocean Ridges. Mid-ocean ridges have relatively high GPE, and the resulting ridge-divergent GPE gives rise to the important "ridge push" force. Large GPE variations occur along the length of the Mid-Atlantic and Arctic ridges as ridge depth, crustal thickness, and mantle buoyancy vary. The greatest influence on ridge GPE variations is effects related to variations in ridge topography, especially in the vicinity of Iceland and Azores. This results from variations in crustal thickness and mantle buoyancy [*Dietrick et al.*, 1995], which each contribute differently to GPE because they have different depths of compensation.

We assume that the sloping ocean floor away from the rift shoulders contributes to ridge push, and that this force is resisted by deformation-related forces near the ridge axis. The magnitudes of the resisting plate boundary forces are relatively small, reflecting the low strength of this boundary. *Neumann and Forsyth* [1993] show that the rift valley and shoulders can be explained with evolving thermal and flexural structure in the rift zone, and that the ridge appears to be in isostatic equilibrium when averaged over the rift valley and shoulders. In this case, the dominant force resisting plate spreading is the work associated with lithospheric extension. When averaging models of 6 and 7 km of crustal thickness, their calculated average tensional stress acting over the 10-km thick plate margin is 10 MPa, which yields a spreading resistance of 10^{11} N per meter of plate margin length (0.1 TN/m). Typical ridge compresses the lithosphere of old ocean with about 4 TN/m [*Turcotte and Schubert*, 1982], indicating that the stress resisting spreading is nearly negligible.

Our calculations of GPE and isostasy are relative to the reference ridge given in Table A2, so that GPE=0 in Fig. A3 is that of the reference ridge. Reference ridge depth is 2.5 km, and we use a 6-km thick crust of average crustal density 2800 kg/m^3. This crustal density is an average of *Dietrick et al.* [1995], *Ito and Lin* [1995] and *Magde et al.* [1995] away from the immediate vicinity of the spreading center. Mantle density is inferred from the mid-Atlantic thermal modeling of *Neumann and Forsyth* [1993, their Fig. 7] for 1.5 m.y. old crust. This age is obtained by noting that the rift shoulder along the Mid-Atlantic Ridge typically is about 15 km from the rift axis, and the half spreading rate averages about 10 mm/yr along the North American plate. We assign a density of 3320 kg/m^3 for uppermost mantle of this temperature based on the density relations of *Christensen and Mooney* [1995]. Assuming a thermal expansion coefficient of 3.4×10^{-5}, we obtain density as a function of depth for the *Neumann and Forsyth* thermal models. We assume an asthenosphere potential temperature of 1350°C, which yields a density of 3218 kg/m^3. The effects of compression on density are ignored since we are interested only in lateral density variations. With seawater of density 1030 kg/m^3, integrated density moment to 125 km gives a GPE of 2.3747×10^{14} N/m. The extensional resistance discussed above has the effect of reducing effective ridge GPE by 10^{11} N/m, yielding a reference ridge potential energy $GPE_0=2.3737\times10^{14}$ N/m above 125 km depth. We include the effects of this tensional stress by filtering the geoid to eliminate wavelengths shorter than 400 km, which diminishes average ridge GPE by 10^{11} N/m. It also has the desirable effect of removing the short-wavelength affects associated with flexural support of loads. Our estimate of ridge reference GPE is not very sensitive to reasonable variations in the values that go into its calculation. Note that GPE varies considerably along the length of the Atlantic and Arctic Ridges, with an Atlantic Ridge GPE between Iceland and Azores that is 1-2 TN/m greater than our reference ridge.

North Atlantic Craton Push. The high calculated North Atlantic GPE shown in Fig. A3 results from the shallow bathymetry and high geoid between Iceland and the Azores, which is due in part to buoyant mantle [e.g., *Dietrick et al.*, 1995]. Geoid response functions predict that upper mantle buoyancy of the wavelengths that dominate the field in the North Atlantic would create a geoid low [e.g., *Richards and Hager*, 1988]. However, buoyant mantle confined by a cratonic root is dynamically isostatic and would create a geoid high over the uplifted sea floor up to the root margin, as is seen in the North Atlantic (Fig. A4a) [*King*, 2005]. Such buoyant upper mantle also would push on the confining root. Thus the North Atlantic geoid and elevation highs are consistent with buoyant upper mantle confined by and pushing on the North American (and Scandinavian) cratonic root. To include this possibility, we include a load acting along the root margin where it is adjacent to the geoid high (as shown in Fig. A4a). If a uniformly buoyant mantle pushed on a root extending to 250 km, it would create twice the push as would a volume of the same net buoyancy extending to 125 km (our assumed depth of compensation in calculations of the long-wavelength GPE). In particular, mantle buoyancy elevating sea floor by 1 km would push on a 250-km deep root with an additional force of 1.4 TN per horizontal meter of root.

Yellowstone Potential Energy. A GPE high is centered over Yellowstone (Fig. A4b), which could be due to buoyant mantle deeper than the 125 km depth of compensation assumed in our calculations of long-wavelength GPE. We include with a load representing additional GPE in the vicinity of Yellowstone. This load is distributed over an area about the size of Wyoming and is centered on Yellowstone, and is applied as horizontal tractions in the direction of the GPE gradient. These tractions form a nearly radial pattern directed away from Yellowstone.

A2.2 Basal Tractions

Our modeling incorporates three basal tractions fields, representing global flow, root drive or drag, and the sum of the torque-balancing tractions. With these we represent in our 2D modeling the effects of sub-lithospheric flow in an Earth possessing a 3D viscosity structure. In particular, the effects of the cratonic root are simplified to including uniform tractions acting on a patch located where the deep root is inferred to exist. The tractions used to represent global flow are derived from a model that used only radial viscosity variation [*Becker and O'Connell*, 2001], and the actual flow field beneath North America certainly will be influenced to some (unknown) amount by the effects of the cratonic root and other lateral viscosity variations.

A2.2.1 Global Flow

Horizontal tractions from *Becker and O'Connell* [2001] (Fig. A4c) are used to incorporate the effect of global mantle flow on the base of North America. This traction field is similar to other models of global flow [e.g., *Steinberger et al*., 2001; *Lithgow-Bertelloni and Guynn,* 2004]. *Becker and O'Connell* [2001] calculated their basal traction field using upper mantle (but below 220 km) and lower mantle density structure derived from tomography models and subduction history, and plate motion. For North America, the sinking Farallon slab beneath the eastern continent creates the dominant tractions [cf., *Lithgow-Bertelloni and Guynn,* 2004]. The magnitude of horizontal traction is sensitive to upper mantle viscosity structure, which is not well understood. As we do with the other loads, we scale this traction field by a multiplicative constant and seek the value that leads to a predicted stress field that best matches the observed stress field.

A2.2.2 Root Drag

Motion between North America lithosphere and the underlying mantle may be relatively coupled at the cratonic root, especially if asthenospheric viscosity is low [*Wesnousky and Scholz*, 1980]. We represent the root by the area where *Grand*'s [1997] S-wave velocity structure averages >3% fast between 50-400 km depth (Fig. A4c). A traction vector of any orientation and magnitude is modeled by applying two orthogonal horizontal loads, one directed NE and the other directed NW.

A2.2.3 Sum Of Drags

As discussed above, each of our applied loads includes the primary load and a torque-balancing basal traction field. The tractions for each load are those that would result if the applied load moved North America over a uniform-viscosity fluid, and are described by an Euler pole. This basal traction field is easily calculated for any set of coefficients that represent the applied loads.

A2.2.4 Tractions Not Modeled

Basal tractions associated with viscous shear coupling near plate margins [e.g., *Silver and Holt*, 2002] are not included explicitly in our model. These are included implicitly because they are in the model of *Becker and O'Connell* [2001], although only in a very diffuse manner because their model contains no information of wavelength shorter that 1300 km (l =31). We tested basal loads that decayed exponentially away from transform and subduction margins with a characteristic length of 200 km to represent plate interaction basal shear tractions, but rejected this load on the grounds that they could not be resolved independently from the margin loads, even in areas where observed stress data are abundant.

In addition to the horizontal tractions discussed above, *Becker and O'Connell* calculate vertical tractions acting on the base of North America. The resulting dynamic topography also creates stresses within the North American plate (see, for instance, discussion by *Lithgow-Bertelloni and Guynn* [2004]). These stresses are included in our GPE calculations because stress caused by dynamic load acting at the base of a plate is the same as that caused by buoyancy located at the same depth (each causing the same uplift). We tried including the effect of the *Becker and O'Connell* vertical tractions and found that their best-fitting amplitude is trivially small and produced no discernible improvement in the fit to observed data.

A2.3 Boundary Loads

Loads are applied to all portions of the North America plate boundary except along the spreading axes (which is handled as discussed above). Loads acting on the plate boundaries are applied as illustrated in Fig. A1.

The Siberia portion of plate margin is represented by a load oriented N45W, roughly normal to the mountainous trend that defines most of this boundary.

Kamchatka loads are applied normal and parallel to a line joining the western end of the Aleutian subduction zone to southern Siberia. This parameterization is meant to represent the loads acting on the Kamchatka subduction zone and Sea of Okhotsk in a simple yet rather general manner, since we have little information on the state of stress south of our arbitrary line.

The Aleutian margin is modeled with four loads. To include the westward increasing component of oblique subduction, one load is parallel to the margin and increases linearly from zero to full value at the western end. Three normal loads are applied, one that tapers from zero to full value going west to east, another tapering in the opposite direction, and a third that is maximum in the center and tapers to zero at either margin. With this set of loads, variations in subduction coupling and plate rollback can be incorporated.

Yakutat block collision with continental North America is modeled as a stress applied in the direction of Pacific plate convergence toward North America. Although short in length, the regional effects of this collision are strong (Fig. 2b) [*Mazzotti and Hyndman et al*., 2002; *Hyndman et al*., 2005].

The Queen Charlotte Fault is modeled with three loads, margin normal and parallel loads north of Vancouver Island (N53), and a separate fault-normal (N40E-directed) load on the fault south of N53, where the transform Queen Charlotte Fault is strongly restraining in orientation.

The Cascadia subduction zone is modeled with a Cascadia parallel load and with north and south Cascadia normal loads.

The San Andreas Fault is represented by fault normal and parallel loads.

Gulf of California transform faults are represented by fault normal and parallel loads.

Mid-America subduction is represented by two loads oriented in the direction of plate convergence, one that tapers linearly to zero at the north end, and the other that tapers to zero at the south end.

The Caribbean transform margin is represented by fault normal and parallel loads.

The Puerto Rico subduction zone is represented by a load oriented N85E, in the direction of relative plate motion. Although short in length, subduction at Puerto Rico is associated with old, slowly subducting plate and a very deep trench.

The South America plate boundary is represented by a normal load. We tested a margin-parallel load, but found it to be negligible in magnitude.

A3. Modeling

Through repeated summing of weighted basis stress fields we seek the set of coefficients that best predict the observed stresses under the measure of misfit shown in Fig. A5. Best-fitting models are found using a simulated annealing algorithm, where we repeat the search many times with different initial estimates. With each GPE field, searches always converge on the same solution, suggesting that the solutions are global minimums. Minor variations in the form of this misfit function have little effect, as judged by visual inspection. Similarly, the models with misfits nearly as low as the minimum-misfit model have scaling coefficients not much different from the minimum-misfit model. We find most scaling coefficients can be altered by up to 30% and, with appropriate adjustment of other scaling coefficients, an acceptable model can be found (based on visual appearance). However, the range in acceptable models is not great. This is because the effect of any particular load is strongest local to the site of application, and it usually is not possible to create this local stress with the more remote fields. Through the trial of millions of coefficient sets, and using a variety of GPE estimates, no acceptable solutions are found that deviate strongly from the results shown in Fig. A6. Thus we think that the actual load distribution on the North American plate is in the vicinity of this solution. Table A3 lists the misfit for best-fit models calculated for the various GPE estimates and for cases that include and exclude root drag effects. Fig. 4 and Table A4 show the coefficients found for the three best models, which include root drag and correspond to GPE estimates using crossover wavelengths of 600, 1250 and 2500 km. These three models fit the stress observations similarly well and are distinctly better than the other models (Table A3). In particular, the stresses on the Queen Charlotte fault and across Siberia need to be artificially bounded for most other models, and only the best three models account well for the observed stresses in the southern Rocky Mountains.

Fig. A6 shows our preferred model. This model has a GPE estimate derived with a 1250-km crossover wavelength, which is intermediate to the other two best models, and it has the most moderate set of boundary loads among all models.

During the search for the best set of scaling coefficients, limits were imposed to keep coefficient values from exceeding realistic values (see Fig. 3). We restrict boundary shear to be of the sign known to occur (e.g., San Andreas shear is right lateral). We also restrict the push of buoyant North Atlantic mantle on the cratonic root to have a value between zero and the full effect of 1.4 TN/m, as discussed in the Tectonic Loads section above. The constraint of greatest effect is the limit on the level of compression at the site of Yakutat collision, which we cap at 6 TN/m. Without this cap, compression levels exceeding 12 TN/m would improve the model fit to the data. Very compressive tectonics result from subduction of an ocean plateau and associated continental fragments at Yakutat [*Mazzotti and Hyndman*, 2002], but we judge values greater than 6 TN/m to be unrealistically large. The tendency of modeling to prefer such great values results from several effects that complicate stress in the local area, including a probable decoupling between upper crust and upper mantle stress in the region [*Mazzotti and Hyndman*, 2002] and the basal tractions resulting from plateau subduction being distributed over a large area north of the plate margin. Because these effects are poorly modeled in 2D, we choose a load magnitude cap that creates approximately north-oriented maximum horizontal compression, and then proceed without concern for obtaining the best-possible fit to the observed stress in this area.

A4. Errors

Overall error is difficult to assess accurately. The problem lies not in the formal treatment of model uncertainty, but rather in the more problematic issues of understanding data quality and its effects on model parameter estimation.

With respect to our representation of the North America stress field, Fig. A7 shows model parameter covariance for our best model. Fig A7a shows the diagonal-normalized second-derivative matrix of the measured misfit for all pairs of basis functions (except GPE and Yakutat, which are held fixed), evaluated about the best solution. Most model parameters, by being isolated, are found to be insensitive to other model parameters. The normal stresses along the western margin of North America are exceptional in their mutual sensitivity on each other. Fig. A7b shows the eigenvectors of the second-derivative matrix, and this figure provides a better sense of model-parameter resolvability. Most eigenvectors are dominated by a single or few basis stress fields, and most basis stress fields are linearly independent from most others. For instance, NE root drag is isolated and robust, whereas NW root drag is only moderately well isolated and it contributes to several eigenvectors. Also, the nature of model-parameter trade-off for the western margin normal loads is more clearly represented in the eigenvector plot. For instance, the normal loads to the Queen Charlotte and southern Cascadia margins are each seen to contribute importantly to three eigenvectors, and our ability to resolve these loads independently of other loads is compromised.

Another source of error is our simplified and parameterized representation of North America. We argue above, as have many before, that plate-scale dynamics can be modeled well in 2D with a viscous or elastic representation. Also, our segment-wise representation of the boundary loads is both reasonable and effective (e.g., Fig. A7), although details of the stress field near the plate margin are not resolvable.

Potential problems with the stress data are discussed above. Away from problematic areas such as subduction zones and near-shore sediment piles, the stress data are thought to be representative of plate stress. The main problem is an absence or near absence of stress data for large portions of the North American plate.

Our estimation of GPE also is a source of error. We have been careful in our treatment this field, and have modeled six cases each based on separate GPE estimates. Our major problem is resolving the long-wavelength GPE field, which depends on a seismic-based estimate of density structure [*Laske and Masters*, 2002] and an assumed depth of compensation for that portion of the crustal density structure that is not isostatic (unlike *Lithgow-Bertelloni and Guynn* [2004] we find that the Crust 2.0 density structure is nearly isostatic). In the actual Earth, the depth of compensation may have an important long-wavelength component. The resolution of a North Atlantic push on the North America craton (which is a well isolated eigenvector) and Yellowstone (which is a well isolated but very small eigenvector) suggests that these deep buoyancy structures are affecting stress within the North American plate.

To represent net model parameter uncertainty, we use the range of model parameters estimated for the three best models. That is, assuming we have resolved root drag and that GPE estimates of crossover wavelength greater than 2500 km are relatively erroneous, we are left with the three models in the upper left corner of Table A3. Understanding that this is a small sample, we arbitrarily add 0.5 TN/m to the uncertainty for each eigenvector that shares a basis stress field (with a second normalized value over 0.4 in Fig A7b), and then add 0.5 TN/m to all estimates. For basis function load given in MPa, we add 0.5 MPa plus 0.5 MPa for

each shared eigenvector; for values in percent, we add 10% plus 10% for each shared eigenvector. These uncertainties are shown as error bars on Fig. A6b. Our estimate of uncertainty is thought to represent the actual uncertainties reasonably well, and it is more reasonable than the very small values found through more formal approaches.

A5. Results

A5.1 Potential Energy

Figure A3 shows GPE estimated under different assumptions on the weight given to geoid and seismic information when calculating the GPE. Regardless of GPE model, the North America GPE field drives extension along the North Atlantic Ridge and along the western North American Cordillera, and it drives contraction in the deep oceans, Hudson Bay and across eastern U.S. Also clear is the fact that mid-ocean ridge GPE varies considerably along the length of the ridge, with ridge between Iceland and Azores being 1-2 TN/m higher than our reference ridge, and the Arctic Ridge being about 1 TN/m lower than our reference ridge.

The misfit of our stress model depends moderately on the GPE field used (Table A3), although with few exceptions the values of scaling coefficients are not greatly influenced. The best models have crossover wavelengths of 600-2500 km. GPE estimates of longer wavelength crossover appear to incorporate signal from the lower mantle Farallon slab (Fig. A3) and they result in resolvably inferior fits to the stress observations (Table A3). The 1250-km crossover is our favored representation. A single map of best-estimated GPE estimate would add to this GPE estimate the contributions representing our best estimates for Yellowstone and North Atlantic GPE contributions. Figure A3 shows that with increasing crossover wavelength the western U.S. GPE high shifts increasingly toward Yellowstone. This is consistent with Fig. 3, which shows that for increasing crossover wavelength the coefficient scaling Yellowstone-area GPE decreases in value. Figure 6 shows our best estimate for western U.S. GPE, in which we add 24% of the Yellowstone GPE field to the 1250-km crossover GPE field (24% being the Yellowstone scaling coefficient for the model using a 1250-km cross-over GPE field).

A5.2 Basal Tractions

Tests run with and without tractions applied on the cratonic root show that omission of the root significantly degrades measured misfit to the observed data (Table A3), but that it does not greatly change the overall distribution of the boundary loads. The value of root basal traction for the best-fit models is 4-5 MPa directed NE-NNE, with this traction applied to the 2.6×10^6 km² area shown in Fig. A4 (this area is ~5% of North America plate area). Fig. A7 indicates that the NE-oriented component of root drag is independent of the other loads, suggesting that it is well resolved. The effect of root drag is the creation of a stress contribution that tends to counteract ridge push and place western U.S. in a "stress shadow" that is less compressed by ridge push than regions to the north or south.

Inclusion of plate-wide basal tractions derived from the *Becker and O'Connell* [2001] global flow model always improves the fit. The absolute value of these tractions is ~5-50% of the values inferred from this model (Table A3), implying that the viscosity ratio of the uppermost mantle to the lower mantle is lower than that assumed by *Becker and O'Connell* [2001]. Our best three models all have basal tractions at ~20% of the *Becker and O'Connell* values. Considering the large uncertainties in knowledge of Earth's radial viscosity structure, an estimate for a different magnitude of these basal tractions is not especially surprising. However, it should be recognized we have included the 3D nature of Earth's viscosity structure by simply combining results from a 1D model (i.e., that of *Becker and O'Connell* [2001]) with a simple parameterization for the effects of a cratonic root. A better resolution of the magnitude and effects of basal tractions require the testing of more realistic 3D Earth models.

A5.3 Boundary Loads

With the exception of subduction margins, loads on the margin of North America tend to be compressive compared to the reference ridge. A strong outward pull on North America occurs at subduction zones near Puerto Rico (~4 TN/m), southern Cascadia (3.5±1.5 TN/m) and mid-Aleutian trench (2.5±1 TN/m), and subduction forces are compressional in the north Cascades (2±1.5 TN/m), and north Mid-America (1.5±1.5 TN/m) subduction zones. Strong compression occurs at sites of continental and ocean plateau convergence (i.e., Siberia (2-3 TN/m) and Yakutat), and where the South American plate converges on the

North American plate without subduction occurring (~3 TN/m). Fault-normal stresses at transform boundaries usually compresses North America with an average load of ~1 TN/m. This compression is approximately equal to that supplied by average Mid-Atlantic Ridge (which averages about 1 TN/m above our reference ridge). The level of transform-normal compression varies with location, however, and the transform faults in the Gulf of California are slightly tensional (1±1.5 TN/m) compared to the reference ridge. Transform shear loads vary between 0.5-2.5 TN/m. For the Queen Charlotte fault, the absence of isolated eigenvectors (Fig. A7) and a large variation in scaling coefficient values for the various models (Fig. 3) suggest that these loads are not well constrained by the modeling.

References

Anders, M. H., and N. H. Sleep (1992), Magnatism and extension: The thermal and mechanical effects of the Yellowstone hotspot., *J. Geophys. Res., 97*, 15,379–15,393.

Argus, D.F., and R.G. Gordon (1991), Current Sierra Nevada-North America motion from very long baseline interferometry; implications for the kinematics of the Western United States, *Geology, 19,* 1085—1088.

Atwater, T. (1970), Implications of plate tectonics for the Cenozoic evolution of western North America, *Geol. Soc. Am. Bull., 81*, 3513–3536.

Atwater, T. and J.M. Stock (1998), Pacific-North America plate tectonics of the Neogene Southwestern United States: An Update, *Int. Geol. Rev., 40*, 375–402.

Armstrong, R. L., and Ward, P. (1991), Evolving geographic patterns of Cenozoic magmatism in the North American Cordillera: The temporal and spatial association of magmatism and metamorphic core complexes, *J. Geophys. Res., 96*, 13,201–13,224.

Bassin, C., G. Laske, and G. Masters (2000), The current limits of resolution for surface wave tomography in North America, *EOS Trans. AGU*, *81*, F897.

Becker, T. W. and R. J. O'Connell (2001), Predicting plate velocities with mantle circulation models, *Geochem., Geophys., Geosystems, 2*, 2001GC000171.

Bennett, R.A., J.L. Davis, B.P. Wernicke (1999), Present-day pattern of Cordilleran deformation in the western United States, *Geology*, 27, 371-374.

Bennett, R.A., B.P. Wernicke, N.A. Niemi, A.M. Friedrich, and J.L. Davis (2003), Contemporary strain fields in the northern Basin and Range province from GPS data, *Tectonics, 22*, 1008, doi:10.1029/2001TC001355.

Bercovici, D. (1995), On the purpose of toroidal motion in a convecting mantle, *Gepohys. Res. Lett., 22,* 3107–3110.

Bercovici, D. (2003), The generation of plate tectonics from mantle convection, *Earth Planet. Sci. Lett., 205*, 107–121.

Beroza, G., and T. Mikumo, Short slip duration in dynamic rupture in the presence of heterogeneous fault properties, *J. Geophys. Res., 101*, 22,449-22,460.

Bird, A., G. Rogers and G. Spence (1995), Earthquakes in the Queen Charlotte Islands Region 1984–1996, http://www.litho.ucalgary.ca/publications/newsletter10.1/bird.html.

Bird, P. (1996), Computer simulations of Alaskan neotectonics, *Tectonics, 15*, 225–336.

Bird, P. (1998), Testing hypotheses on plate-driving mechanisms with global lithosphere models including topography, thermal structure and faults*, J. Geophys. Res., 103*, 10,115–10,129.

Bird, P. and X. Kong (1994), Computer simulations of California tectonics confirm very low strength of major faults, *Geol. Soc. Am. Bull., 106*, 159–174.

Bird, P. and Y. Li (1996), Interpolation of principal stress directions by nonparametric statistics: Global maps with confidence limits, *J. Geophys. Res., 101*, 5435–5443.

Bird, P. and K. Piper (1980), Plane-stress finite-element models of tectonic flow in southern California, *Phys. Earth Planet. Interiors*, *21*, 158–175.

Bird, P., and R. W. Rosenstock (1984), Kinematics of present crust and mantle flow in southern California, *Geol. Soc. Am. Bull., 95,* 946–957.

Bokelmann, G. H. R. (2002a), What forces drive North America?, *Geology., 30*, 1027–1030.

Bokelmann, G. H. R. (2002b), Convection-driven motion of the North American craton: Evidence from P-wave anisotropy, *Geophys. J. Int., 148*, 278–287.

Bostock, M. and J. Vandecar (1995), Upper mantle structure of the northern Cascadia subduction zone. *Can. J. Earth. Sci.*, 32: 1–12.

Brandon, M. T., M. K. Rode-Tice and J. J. Garver (1998), Late Cenozoic exhumation of the Cascadia accretionary wedge in the Olympic Mountains, NW Washington State, *Geol. Soc. Am. Bull., 110*, 985–1009.

Bunge, H. P. and S. P. Grand (2000), Mesozoic plate-motion history below the northeast Pacific Ocean from seismic images of the subducted Farallon slab, *Nature, 405*, 337–340.

Burchfiel, B. C., D. S. Cowen, and G. A. Davis (1992), Tectonic overview of the Cordilleran orogen in the western United States, in *The Cordilleran Orogen: Conterminous U.S.*, vol. G-3, pp. 407–479, edited by B. C. Burchfiel, P. Lipman and M. L. Zoback, Geological Society of America, Boulder, CO.

Choi, E-s, and M. Gurnis (2003), Deformation in transcurrent ane extensional environments with widely spaced weak zones, *Geophys. Res. Lett., 30*,doi: 1–4, 10.1029/2002GRL016129 .

Christensen, N. I. and W. D. Mooney (1995), Seismic velocity structure and composition of the continental crust: A global view, *J. Geophys. Res., 100*, 9761–9788.

Christiansen, R. L. and R. S. Yeats (1992), Post-Laramide geology of the U.S. Cordilleran region, in *The Cordilleran Orogen: Conterminous*

U.S., vol. G-3, pp. 261–406, edited by B. C. Burchfiel, P. Lipman and M. L. Zoback, Geological Society of America, Boulder, CO.
Coblentz, D. and R. Richardson (1996), Analysis of the South American intraplate stress field, *J. Geophys. Res., 101*, 8643–8657.
Coney, P. J. (1980), Cordillerian metamorphic core complexes: An overview, in *Cordillerian metamorphic core complexes*, edited by M. D. Crittendon, P. J. Coney, G. H. Davis, *Geological Soc. Am. Mem. 153*, 7–31.
Coney, P. J., and T. A. Harms (1984), Cordilleran metamorphic core complexes: Cenozoic extensional relics of Mesozoic compression, *Geology, 12*, 550–554.
Coney, P. J., and S. J. Reynolds (1977), Flattening of the Farallon slab, *Nature, 270*, 403–406.
Conrad, C. P., C. Lithgow-Bertelloni and K. E., Louden (2004), Iceland, the Farallon slab, and dynamic topography of the North Atlantic, *Geology*, *32*, 177–180; doi: 10.1130/G20137.1.
Crosson, R.S. and T.J. Owens (1987), Slab geometry of the Cascadia subduction zone beneath Washington from earthquake hypocenters and teleseismic converted waves, *Geophys. Res. Lett., 14*, 824–827.
Detrick, R. S., H. D. Needham and V. Renard (1995), Gravity anomalies and crustal thickness variations along the Mid-Atlantic Ridge between 33°N and 40°N, *J. Geophys. Res., 100*, 3767–3787.
Dickinson, W.R., C.A. Hopson, and J.B. Saleeby (1996), Alternate origins of the Coast Range Ophiolite (California): Introduction and implications, *GSA Today, 6*, 1–10.
Dixon, T.H., M. Miller, F. Farina, H.Z. Wang, and D. Johnson, Present-day motion of the Sierra Nevada block and some tectonic implications for the Basin and Range province, North American Cordillera, *Tectonics, 19*, 1–24, 2000.
Ducea, M.N., and J.B. Saleeby, J.B. (1996), Buoyancy sources for a large, unrooted mountain range, the Sierra Nevada, California; evidence from xenolith thermobarometry, *J. Geophys. Res., 101*, 8229–8244.
Duncan, R. (1982), A captured island chain in the Coast Range of Oregon and Washington, *J. Geophys. Res., 87*, 10,827–10,837.
Eaton, J. E. (1932), Decline of the Great Basin, southwest United States, *Bull. Am. Ass. Pet. Geo., 16,* 1-22.
Elsasser, W. M. (1969), Convection and stress propagation in the upper mantle, in *The application of modern physics to the Earth and planetary interiors*, edited by S. K. Runcorn, Wiley-Interscience, London, 223–246.
Fleitout, L. (1991), The Sources of Lithospheric Tectonic Stresses, *Phil. Trans. Royal Soc. London, Ser. A, 337*, 37–81.
Fleitout, L. and C. Froidevaux (1982), Tectonics and topography for a lithosphere containing density heterogeneities, *Tectonics, 1*, 21–56.
Flesch, L. M., W. E. Holt and A. J. Haines (2001), Dynamics of the India-Eurasia collision zone, *J. Geophys. Res., 106*, 16,435–16,460.
Flesch, L. M., W. E. Holt, A. J. Haines and B. Shen-Tu (2000), Dynamics of the Pacific-North American Plate Boundary in the Western United States, *Science, 287*, 834–836.
Forsyth, D.W and S. Uyeda (1975), On the relative importance of the driving forces of plate motion, *Geophys. J.R. Astro. Soc., 43*, 163–200.
Forte, A. M. and J. X. Mitrovica (2001), Deep-mantle high viscosity flow and thermo-chemical structure inferred from seismic and geodynamic data, *Nature, 410*, 1049–1056.
Fouch, M. J., K. M. Fischer, E. M. Parmentier, M. E. Wysession and T. J. Clarke (2000), Shear wave splitting, continental keels, and patterns of mantle flow, *J. Geophys. Res., 105*, 6255–6275.
Gao, W., S. Grand, W.S. Baldridge, D. Wilson, M. West, J. Ni, and R. Aster (2004), Upper mantle convection beneath the central Rio Grande rift imaged by P and S wave tomography, *J. Geophys. Res., 109*, B03305, doi:10.1029/2003JB002743.
Geist, E. L. (1996), Relationship between the present-day stress fields and plate boundary forces in the Pacific Northwest, Ge*ophys. Res. Lett., 23,* 3381–3384.
Gordon, R. G. (1998), The plate tectonic approximation: Plate nonrigidity, diffuse plate boundaries, and global plate reconstructions. *Ann. Rev. Earth Planet. Sci.*, *26*, 615–642.
Govers, R. and P. T. Meijer (2001), On the dynamics of the Juan de Fuca plate, *Earth Planet. Sci. Lett., 189*, 115–131.
Gripp, A. E., and R. G. Gordon (2002), Young tracks of hotspots and current plate velocities, *Geophys. J. Int., 150*, 321–361.
Grand, S. P. (1994), Mantle shear structure beneath the Americas and surrounding oceans, *J. Geophys. Res., 99*, 11,591–11,621.
Grand, S. P., R. D. van der Hilst and S. Widiyantoro (1997), Global seismic tomography: A snapshot of convection in the Earth, *GSA Today, 7*, no. 4, 1–7.
Gurnis, M. (1992), Rapid continental subsidence following the initiation and evolution of subduction, *Science 255,* 1556–1558.
Hammond, W. C., and W. Thatcher (2004), Contemporary tectonic deformation of the Basin and Range province, western United States: 10 years of observation with the Global Positioning System, *J. Geophys. Res., 109,* B08403, doi:10.1029/2003JB002746.
Hammond, W.C., and Thatcher W., Northwest basin and range tectonic deformation observed with the global positioning system, 1999-2003, *J. Geophys. Res., 110*, B10405, 2005.
Hansen, K. M. and V. S. Mount (1990), Smoothing and extrapolation of crustal stress orientation measurements, *J. Geophys. Res., 95*, 1155–1165.
Harris, A. R., H. M. Iyer, and P. B. Dawson (1991), Imaging the Juan de Fuca plate beneath southern Oregon using teleseismic P wave residuals, *J. Geophys. Res., 96*, 19,879 – 19,889.
Haxby, W. F. and D. L. Turcotte (1978), On isostatic geoid anomalies, *J. Geophys. Res., 83*, 5473–5478.
Henry, C.D., and J.J. Aranda-Gomez (2000), Plate interactions control middle-late Miocene, proto-Gulf and Basin and Range extension in southern Basin and Range, *Tectnophysics, 318*, 1–26.
Heaton, T. H. (1990), Evidence for and implications of self-healing pulses of slip in earthquake rupture, *Phys. Earth Planet. Interiors, 64*, 1–20.
H G. Hirth, D.L. Kohlstedt (1996), Water in the oceanic upper mantle: implications for rheology, melt extraction and the evolution of the lithosphere, *Earth Planet. Sci. Lett. 144*, 93–108.
Houseman, G. A., E. A. Neil, and M. D. Kohler (2000), Lithospheric instability beneath the Transverse Ranges of California, *J. Geophys. Res., 105*, 16237–16250.
Humphreys, E. (1995), Post-Laramide removal of the Farallon slab, western United States, *Geology, 23,* 987–990.
Humphreys, E., E. Hessler, K. Dueker, E. Erslev, G. L. Farmer and T. Atwater (2003), How Laramide-age hydration of North America by the Farallon slab controlled subsequent activity in the western U.S., *Int. Geology Rev., 45*, 575–595.

Humphreys, E., and B. Hager (1990), A kinematic model for the late Cenozoic development of southern California crust and upper mantle, *J. Geophys. Res., 95*, 19,747–19,762.
Humphreys, E., and R. Weldon, Deformation across the western United States: A local estimate of Pacific-North America transform deformation, *J. Geophys. Res., 99*, 19,975–20,010, 1994.
Hunt, A. G. and P. E. Malin (1998), Possible Triggering of Heinrich Events by ice-load induced earthquakes, *Nature, 393*, 156–158.
Hyndman, R., P. Fluck, T., Mazzotti, T. Lewis, J. Ristau and L. Leonard (2005), Current Tectonics of the Northern Canadian Cordillera. *Can. J. Earth Sciences*, *42*, 1117–1136.
Ito, G., J. Lin, and D. Graham (2003), Observational and theoretical studies of the dynamics of mantle plume–mid-ocean ridge interaction, *Rev. Geophys., 41(4),* 1017, doi:10.1029/2002RG000117.
Ito, G. T. and J. Lin (1995), Mantle temperature anomalies along the past and paleoaxes of the Galapagos spreading center as inferred from gravity analyses, *J. Geophys. Res., 100*, 3733–3745.
Jackson, J. (2002), Strength of the continental lithosphere: Time to abandon the jelly sandwich?, *GSA Today, 12,* no. 9, 4–10.
Jackson, J. (2002), Faulting, Flow, and the Strength of the Continental Lithosphere, *Int. Geology Rev., 44,* 39–61.
Jones, C. H., G. L. Farmer, and J. R. Unruh (2004), Tectonics of Pliocene removal of lithosphere of the Sierra Nevada, California, *Geol. Soc. Am. Bull.*, *116*, 1408–1422,.
Jones, C. H., L. J. Sonder, and J. R. Unruh (1998), Lithospheric graviational potential energy and past orogenesis: Implications for conditions of initial Basin and Range and Laramide deformation, *Geology*, *26*, 639–642.
Jones, C. H., J. R. Unruh and L. J. Sonder (1996), The role of gravitational potential energy in active deformation in the southwestern United States, *Nature, 381*, 37–41.
Jordan, B. T.**,** A. L. Grunder, R. A. Duncan and A. L. Deino (2004), Geochronology of age-progressive volcanism of the Oregon High Lava Plains: Implications for the plume interpretation of Yellowstone: *J. Geophys. Res., 109*, B10202, doi:10.1029/2003JB002776.
Kanamori, H. (1994), Mechanics of Earthquakes: *Ann. Rev. Earth Planet. Sci., 22*, 207–237.
King, S. D. (2005), North Atlantic topographic and geoid anomalies: The result of a narrow ocean basin and cratonic root?, in *Plates, Plumes & Paradigms,* edited by G. R. Foulger, D. L. Anderson, J. H. Natland, D. C. and Presnall, Geological Society of America Special Paper 388, 653–664.
Kohlstedt, D. L., B. Evans, and S. J. Mackwell (1995), Strength of the Lithosphere: Constraints Imposed by Laboratory Experiments, *J. Geophys. Res. 100*, 17,587–17,602.
Kreemer, C, J. Haines, W. E. Holt, G. Blewitt, and D. Lavallee (2000), On the determination of a global strain rate model, *Earth Planets Space, 52*, 765–770.
Kreemer, C., W.E. Holt, A.J. Haines, An integrated global model of present-day plate motions and plate boundary deformation, Geophy. J. Int., 154 (1), 8–34, 2003.
Laske, G. and G. Masters, Crust 2.0 Web Page, http://mahi.ucsd.edu/Gabi/rem.html, 2002.
Lewis, J. C., J. R. Unruh, and R. J. Twiss (2003), Seismogenic strain at the Cascadia convergent margin, *Geology*, *31*, 183–186.
Lithgow-Bertelloni, C. and J. H. Guynn (2004), Origin of the lithospheric stress field, *J. Geophys. Res., 109*, B01408, doi:10.1029/2003JB002467.
Lithgow-Bertelloni, C. and M. A. Richards (1998), The dynamics of Cenozoic and Mesozoic plate motions, *Rev. Geophys., 36*, 27–78.
Liu, M. (2001), Cenozoic extension and magmatism in the North America Cordillera: the role of gravitational collapse, *Tectnophysics, 342*, 407–433.
Liu, M., and Y. Shen (1998), Crustal collapse, mantle upwelling, and Cenozoic extension in the North America Cordillera, *Tectonics, 17*, 311–321.
Liu, Z. and P. Bird (2002), North America plate is driven westward by lower mantle flow, Ge*ophys. Res. Lett., 29,* doi: 10.1029/2002GRL016002.
Livaccari, R. (1991), Role of crustal thickening and extensional collapse in the tectonic evolution of the Sevier-Laramide orogeny, western United States, *Geology, 19*, 1104–1107.
Lowry, A. R., N. M. Ribe, and R. B. Smith (2000), Dynamic elevation of the Cordillera, western United States, *J. Geophys. Res*., *105*, 23,371–23,390.
Lowry, A. R. and R. B. Smith (1995), Strength and rheology of western U.S. Cordillera, *J. Geophys. Res., 100*, 17,947–17,964.
Magde, L. S., R. S. Detrick and the TERA Group (1995), Crustal and upper mantle contribution to the axial gravity anomaly at the southern East Pacific Rise, *J. Geophys. Res., 100*, 3747–3766.
Mann, P. (1997), Model for the formation of large, transtensional basins in zones of tectonic escape, *Geology 25*, 211–214.
Mazzotti, S and R. Hyndman (2002), Yakutat collision and strain transfer across the northern Canadian Cordillera, *Geology, 30*, 495–498.
McCaffrey R., Block kinematics of the Pacific-North America plate boundary in the southwestern United States from inversion of GPS, seismological, and geologic data, J. Geophys. Res., 110, B07401, doi:10.1029/2004JB003307, 2005.
McClusky, S.C., S.C. Bjornstad, B.H. Hager, R.W. King, B.J. Meade, M.M. Miller, F.C. Monastero, and B.J. Souter, Present day kinematics of the Eastern California Shear Zone from a geodetically constrained block model, *Geophys. Res. Lett., 28*, 3369–3372, 2001.
Miller, M.M., D.J. Johnson, T.H. Dixon, and R.K. Dokka, Refined kinematics of the Eastern California shear zone from GPS observations, 1993-1998, *J. Geophys. Res., 106*, 2245–2263, 2001.
Minster, J. B, T. H. Jordan, P. Molnar and E. Haines (1974), Numerical modeling of instantaneous plate tectonics, *Geophys. J.R. Astron. Soc. 36*, 541–576.
Molnar, P. and H. Lyon-Caen (1988), Some simple physical aspects of the support, structure, and evolution of mountain belts, Spec. Pap. *Geol. Soc. Am*., *218*, 179–207.
Morgan, J. P., W. J. Morgan, Y.-S. Zhang, and W. H. F. Smith (1995), Observational hints for a plume-fed, sub-oceanic asthenosphere and its role in mantle convection, *J. Geophys. Res., 100*, 12,753–12,767.
Neumann, G. A. and D. W. Forsyth (1993), The paradox of the axial profile: Isostatic compensation along the axis of the Mid-Atlantic

Ridge?, *J. Geophys. Res., 98*, 17,891–17,910.
Nunn, J. A. (1985), State of stress in the northern Gulf Coast, *Geology, 13*, 429–432.
Oldow, J. S. (2003), Active transtensional boundary zone between the western Great Basin and Sierra Nevada block, western US cordillera, *Geology, 31*, 1033–1036.
Page, R. A., N. N. Biswas, J. C Lahr and H. Pulpan (1991), *Seismicity of continental Alaska, in Neotectonics of North America*, Decade Map Vol. l, edited by D. B. Slemmons, E. R. Engdahl, M. D. Zoback and D. D. Blackwell, Geological Society of America, Boulder, Colorado.
Panasyuk, S. V., and B. H. Hager (2000), Inversion for mantle viscosity profiles constrained by dynamic topography and the geoid, and their estiamted errors, *Geophys. J. Int., 143*, 821–836.
Parsons, T., G. A. Thompson, and N.H. Sleep (1994), Mantle plume influence on the Neogene uplift and extension of the U.S. western cordillera *Geology, 22*, 83–86.
Priest, G. R. (1990), Volcanic and tectonic evolution of the Cascades volcanic arc, central Oregon, *J. Geophys. Res., 95,* 19,583–19,599.
Provost, A.-S. and H. Houston (2003), Constraints from stress orientations on the evolution of frictional strength along the San Andreas fault, *J. Geophys. Res., 108*, ETG 13-1, 2175, B3, doi:10.1029/2001JB001123.
Rasmussen, J. and E. Humphreys (1988), A tomographic image of the mantle beneath Washington, *Geophys. Res. Lett., 15*, 1417–1420.
Reidel, S. P., K. R. Fecht, M. C. Hagood, L. and Tolin (1989), The geologic evolution of the central Columbia Plateau, in *Volcanism and tectonism in the Columbia River flood-basalt province*, edited by S. P. Reidel and P. R. Hooper, Geol. Soc. Am. Special Paper 239, p. 247–264.
Reinecker, J., O. Heidbach, M. Tingay, P. Connolly and B. Miller (2004), The 2004 release of the World Stress Map (available online at www.world-stress-map.org).
Reynolds, S.D., Coblentz, D. and Hillis, R. (2002), Tectonic forces controlling the regional intraplate stress field in continental Australia: Results from new finite-element modeling: *J. Geophys. Res., B107*, B7, doi:10.1029/2001JB000408.
Richards, M. A. and B. H. Hager (1988), The Earth's geoid and the large-scale structure of mantle convection, in, *The physics of the planets: their origin, evolution and structure*, edited by S. K. Runcorn, John Wiley & Sons, Chichester, United Kingdom.
Richardson, R. M. and L. M. Reding (1991), North American plate dynamics, *J. Geophys. Res., 96*, 12,201–12,223.
Richardson, R. M. S. C. Soloman, and N. H. Sleep (1976), Intraplate stress as an indicator of plate tectonic driving forces, *J. Geophys. Res., 81*, 1847–1856.
Roy, M., and L. H. Royden (2000a), Crustal rheology and faulting at strike-slip plate boundaries: 1. An analytic model, *J. Geophys. Res., 105*, 5583–5597.
Roy, M., and L. H. Royden (2000b), Crustal rheology and faulting at strike-slip plate boundaries: 2. Effects of lower crustal flow, *J. Geophys. Res., 105*, 5599–5613.
Rubin, A.M. (1995), Propagation of magma-filled cracks, *Ann. Rev. Earth Planet. Sci*., *23*, 287–336.
Saltus, R.W., and Lachenbruch, A.H. (1991), Thermal Evolution of the Sierra Nevada: Tectonic Implications of New Heat Flow Data, *Tectonics, 10*, 325–344.
Saltzer, R. L., and E. D. Humphreys (1997), Upper mantle P-wave structure of the eastern Snake River Plain and its relationship to geodynamic models of the region, *J. Geophys. Res., 102*, 11,829–11,841.
Sauber, J. W. Thatcher, S.C. Solomon, and M. Lisowski (1994), Geodetic slip rate for the eastern California shear zone and the recurrence time of Mojave desert earthquakes, *Nature*, *367*, 264–266.
Saucier, F., E. Humphreys and R. J. Weldon (1992), Stress near geometrically complex strike-slip faults: application to the San Andreas fault at Cajon Pass, southern California, *J. Geophys. Res., 97*, 5081–5094.
Schaff, D., G. Beroza, and B. Shaw (1998), Postseismic response of repeating aftershocks, *Geophys. Res. Lett.*, *25*, 4549–4552.
Scholz, C., (2000), Evidence for a strong San Andreas fault, Geology, 28, 163–166.
Seeber, L., J. G. Armbruster, W.-Y. Kim, N. Barstow and C. Scharnberger (1998), The 1994 Cacoosing Valley earthquakes near Reading, Pennsylvania: A shallow rupture triggered by quarry unloading, *J. Geophys. Res., 103*, 24,505–24,522.
Shen-Tu, B., W.E. Holt and A.J. Haines (1999), The kinematics of the western United States estimated from Quaternary rates of slip and space geodetic data, *J. Geophys. Res, 104*, 28,927–28,955.
Silver, P. G., and W. E. Holt (2002), The mantle flow field beneath western North America, *Science*, *295*,1054–1057.
Simpson, R. W. (1997), Quantifying Anderson's fault types, *J. Geophys. Res., 102*, 17,909–17,919.
Sleep, N. H. (1990), Hotspots and mantle plumes: some phenomenology. *J. Geophys. Res.*, *95*, 6715–6736.
Smith, R. B. (1978), Seismicity, crustal structure, and intraplate tectonics of the Western Cordillera, in *Cenozoic Tectonics and Regional Geophysics of the Western Cordillera*, edited by, R. B. Smith and G. P. Eaton, Memoir 152, Bull. Geol. Soc. Amer., 111–144.
Solomon, S. C., N. H. Sleep and R. M. Richardson (1975), On the forces driving plate tectonics: Inferences from absolute plate velocities and intraplate stress, *Geophys. J. R. Astron. Soc., 42*, 769–801.
Sonder, L. J. and P. C. England (1989), Effects of a temperature-dependent rheology on large-scale continental extension, *J. Geophys. Res, 94*, 7603–7619.
Sonder, L. J., P. C. England, and G. A. Houseman (1986), Continuum calculations of continental deformation in transcurrent environments, *J. Geophys. Res., 91*, 4797–4810.
Sonder, L., and C. Jones (1999), Western Unites States extension: How the west was widened, *Annu. Rev. Earth Planet Sci., 27*, 417–462.
Sonder, L., P. England, B. Wernicke, and R. Christianson (1987), A physical model for Cenozoic extension of western North America, in *Continental extensional tectonics*, edited by Coward, M., et al., *Geol. Soc. London Special Pub. 28*, 187–201.
Spencer, J. E. (1996), Uplift of the Colorado Plateau due to lithosphere attenuation during Laramide low-angle subduction: *J. Geophys. Res., 101*, 13,595–13,609.
Stein, R.S., G.C.P. King and J. Lin (1992), Change in failure stress on the southern San Andreas fault system caused by the 1992 Magnitude=7.4 Landers earthquake, *Science, 258,*. 1328–1332.

Stein, S., N. H. Sleep, R. J. Geller, S-C Wang and G. C. Kroger (1979), Earthquakes along the passive margin of eastern Canada, *Geophys. Res. Lett., 6*, 537–540.
Steinberger, B., H. Schmeling and G. Marquart (2001), Large-scale lithospheric stress field and topography induced by global mantle circulation, *Earth Planet. Sci. Lett., 186*, 75–91.
Svarc, J.L., J.C. Savage, W.E. Prescott, and M.H. Murray (2002a), Strain accumulation and rotation in western Oregon and southwestern Washington, *J. Geophys. Res., 107*, Art. No. 2087.
Svarc, J.L., J.C. Savage, W.H. Prescott, and A.R Ramelli (2002b), Strain accumulation and rotation in western Nevada, 1993-2000, *J. Geophys. Res., 107*, Art. No. 2090.
Sykes, L. R. and M. L. Sbar (1973), Interplate earthquakes, lithospheric stresses, and the driving mechanisms of plate tectonics, *Nature, 245*, 298–302.
Thatcher, W. (2003), GPS constraints on the kinematics of continental deformation, *Int. Geology Rev., 45*, 191–212.
Toomey, D. R., W. S. D. Wilcock, J. A. Conder, D. W. Forsyth, J. Blundy, E. M. Parmentier, and W. C. Hammond (2002), Asymmetric mantle dynamics in the MELT region of the East Pacific Rise, *Earth and Planet. Sci. Lett*., *200*, 287–295.
Townend J., and M. D. Zoback (2004), Regional tectonic stress near the San Andreas fault in central and southern California, *Geophy. Res. Lett., 31*, L15S11.
Turcott, D. L. and G. Schubert (1982), Geodynamics: Applications of continuum mechanics to geological problems, John Wiley and Sons, New York.
Unruh, J., J. Humphrey, and A. Barron (2003), Transtensional model for the Sierra Nevada frontal fault system, eastern California, *Geology*, *31*, 327-330.
Unruh, J. R., and W. R. Lettis (1998), Kinematics of transpressional deformation in the eastern San Francisco Bay region, California, *Geology*, *26*, 19–22.
Wang, K., J. He, and E. Davis (1997), Transform push, oblique subduction resistance, and intraplate stress of the Juan de Fuca plate. *J. Geophys. Res., 102*, 661–674.
Wang, K., T. Mulder, G. Rogers and R. Hyndman (1995), Case for very low coupling stress on the Cascadia subduction fault., *J. Geophys. Res., 100*, 12,907–12,918.
Wells, R. E., C. S. Weaver, R. J. Blakely (1998), Fore arc migration in Cascadia and its neotectonic significance, *Geology, 26*, 759–562.
Wernicke, B. (1992), Cenozoic extensional tectonics of the U.S. Cordillera, in *The Cordilleran Orogen: Conterminous U.S., G-3*, edited by B. P. Burchfiel, P. Lipman and M. L. Zoback, 553–581, Geological Society of America, Boulder, Colorado.
Wernicke, B., and J.K. Snow (1992), Cenozoic tectonism in the central Great Basin: Motion of the Sierran-Great Valley block, *Int. Geol. Rev., 40*, 403–410.
Wesnousky, S. and Scholz, C. (1980), The craton: its effects on the distribution of seismicity and stress in North America, *Earth Planet. Sci. Lett., 48*, 348–355.
Whitehouse, P. L., P. C. England, and G. A. Houseman (2005), A physical model for the motion of the Sierra Block relative to North America, *Earth Planet. Sci. Lett., 237*, 590–600.
Wu, P. (1996), Changes in orientation of near-surface stress field as constraints to mantle viscosity and horizontal stress differences in Eastern Canada, *Geophys. Res. Lett., 23*, 2263–2266.
Zheng, G. and J. Rice (1998), Conditions under which velocity-weakening friction allows a self-healing versus cracklike mode of rupture, *Bull. Seis. Soc. Am., 88*, 1466–1483.
Zhong, S, and M. Gurnis, (1996), Interaction of weak faults and non-Newtonian rheology produces plate tectonics in a 3D model of mantle flow, *Nature, 383*, 245–247.
Zhong, S, M. Gurnis, and L. Moresi (1998), Role of faults, nonlinear rheology and viscosity on structure in generating plates from instantaneous mantle flow models, *J. Geophys. Res., 103*, 15,255–15,268.
Zhong, S, M. Zuber, L. Moresi, and M. Gurnis (2000), Role of temperature-dependent viscosity and surface plates in spherical shell models of mantle convection, *J. Geophys. Res., 105*, 11.063–11.082.
Zoback, M. D., J Townend, and B. Grollimund (2002), Steady-state failure equilibrium and deformation of intraplate lithosphere, *Int. Geology Rev., 44*, 383–401.
Zoback, M. D. (2000), Strength of the San Andreas, *Nature, 405*, 31–32.
Zoback, M. L. (1992), First and second-order patterns of stress in the lithosphere: World Stress Map Project, *J. Geophys. Res., 97*, 11,703–11,728.
Zoback, M. L., and W. D. Mooney (2003), Lithospheric buoyancy and continental intraplate stress, *Int. Geology Rev., 45*, 95–118.
Zoback, M.L., and Thompson, G.A. (1978), Basin and Range rifting in northern Nevada: Clues from a mid-Miocene rift and its subsequent offsets, *Geology, 6*, 111–116.

Figures

Figure 1. Illustration of the forces acting on a plate and the resulting stresses. These are the forces and stresses modeled in our paper. (a) Map view of forces applied to a plate and the resulting plate stresses. Normal and tangential boundary forces (open arrows) are applied along transform and subduction (toothed line) margins. Interior loads (gray arrows) are created by basal tractions and density structure internal to the plate. Black arrows indicate the state of stress created by these forces. (b) Cross section through plate made of continental crust (light gray), ocean crust (black) and mantle lithosphere (dark gray). The plate overlies a sinking mass, which excites mantle flow that creates basal tractions (smaller gray arrows at base of plate and shown in (a) as a radially converging set of forces). Plate motion (relative to the deep Earth) also creates basal tractions (shown with the large gray arrow here and in (a)). In addition, lateral variations in plate density structure give rise to the topography-related forces discussed in (c). (c) Plot of elevation, gravitational potential energy (GPE), and GPE gradient (lower line) across the plate, resulting from the density structure shown in (b). Assuming isostasy, lateral variations in elevation result from lateral variations in the weight of the rock column beneath each location (to a depth of compensation), whereas GPE also depends on the depth distribution of mass within the column, and is greater where elevation is compensated relatively deep. Gradients in GPE create forces in the lithosphere, as illustrated with gray arrows in (b). These forces can be modeled as forces acting on the base of the lithosphere, as illustrated in (a) on the left side and in the ocean basin on the right.

Figure 2. North America observed stress. Maps are Mercator projections about a pole at (15N, 25E), chosen to minimize map distortion. (a) Stress observations from the World Stress Map Project (small symbols, from *Reinecker et al*. [2004]) and other sources (Table A1). Color indicates stress domains: blue for compression, green and gray for strike-slip, and red for tension. Lines on the stress symbols show orientation of maximum horizontal compressive stress SHmax. Western U.S. state boundaries are shown for reference. (b) Stress values used in modeling, derived from averaging the indicators in (a) using the method of *Coblentz and Richardson* [1996]. Values are given in Table A1. Trajectories show SHmax (blue) and SHmin (red) directions estimated using the algorithm of *Hansen and Mount* [1990]. SHmax trajectories are constrained to trend upslope near ridge axes. These trajectories and the colored stress domains are only used as a visual aid, and are not modeled.

Figure 3. Plate loads for the three best gravitational potential energy estimates (cross over wavelengths of 600, 1250 and 2500 km). Solutions are bounded to lie within the white area. Normal stresses are relative to a reference ridge. Patterns show tectonic setting: horizontal rule=collision, diagonal rule=transform, pattern=subduction. Boundary loads given in TN/m. Interior loads are given in MPa for root drag, and as percent of maximum allowed value for North Atlantic push on the craton, Yellowstone GPE and global-flow basal tractions of *Becker and O'Connell* [2001].

Figure 4. Estimated total gravitational potential energy relative to reference ridge (Table A2), as discussed in the Appendix. This is the same figure as the upper right panel in Fig. A3.

Figure 5. Three representative strength profiles with depth-integrated strength equaling 1.6 TN/m, similar to the resolved shear load on the San Andreas plate margin. Regardless of strength profile, mid-crustal shear stress is betweeen the ~300 MPa expected at 18 km depth from rock mechanics experiments (assuming a friction coefficient of 0.6) and typical earthquake stress drops of ~3 MPa.

Figure 6. (a) Western U.S. Geodynamics. Red and blue bars show modeled stress (from Fig A6b), with red indicating tension and blue compression (relative to local pressure). The light-colored area shows where tectonically important deformation is occurring, with Yellowstone (circled Y) at the NE apex. The colored line segments represent active faults (thick for major plate-boundary faults). Gold arrows show velocity relative to North America for the Pacific and Juan de Fuca (JdF) Plates, and for selected points within the deforming western U.S. (including the Sierra Nevada (SN) and Siletzia (S) blocks). Stress trajectories represent the observed stress field (from Fig. 2b, red for tension and blue for compression). (b) Gravitational potential

energy and resulting modeled stresses. The GPE field is composed of the 1250 cross-over wavelength estimate shown in Fig. 3 plus 24% of the Yellowstone GPE, as resolved for the best-fit model using the 1250 cross-over wavelength GPE field (Fig. 4). Contour level is 1 TN/m. Note extension within the regions of high GPE and compression in the regions of low GPE, with the compressive axis oriented with the GPE gradient. In the Basin and Range and California these stresses are responsible for most of the non-strike-slip deformation. (c) Boundary and basal loads and resulting modeled stresses. Loads are from Fig. A6. Note the shear stress field established across California and western Nevada caused by transform interaction, the compression north of California, and the tension common in the western U.S. interior.

Figure A1. Finite element mesh and modeled loads acting on the North American plate. The boundary segments upon which individual boundary loads are applied are shown. Load numbers correspond with those in Fig. 3. Internal loads are shown in Figs. A3 and A4.

Figure A2. Example basis stress fields created by tectonic loads. Colored symbols show principal horizontal stress at the sampled stress locations (Fig. 2b), calculated with the finite element method. Some overlapping symbols have been removed. Blue lines indicate compression and red lines indicate tension. Thick lines are scaled by a factor of four. (a) Stresses caused by gravitational potential energy estimated with a 1250 km cross-over wavelength (see Fig. A3). (b) Stresses caused by a San Andreas normal load of 1 TN/m. (c) Stresses caused by a San Andreas tangential load of 1 TN/m.

Figure A3. Estimated total gravitational potential energy relative to reference ridge (Table A2). Bottom two panels show the gravitational potential energy per unit surface area (GPE) estimated from the geoid and from the Crust 2.0 seismic model [*Laske and Masters*, 2002], where the geoid-based estimate is filtered to pass wavelengths longer than 2500 km and the seismic-based estimate filtered to pass wavelengths shorter than 2500 km. These two fields are then summed to obtain a GPE estimate with a cross-over wavelength of 2500 km. Top four panels show estimated GPE with the cross-over wavelengths indicated. Contour level is 10^{12} N/m (1 TN/m), and black contour is where GPE equals our reference ridge.

Figure A4. Modeled stress fields acting on the base of North American plate. (a) Push of buoyant North Atlantic asthenosphere on cratonic root. Inferred root distribution is represented with the ruled areas, which shows where S-wave velocity across 50-400 km depth interval averages >1% fast in the seismic model of *Grand* [1997]. Also shown is the geoid. The large geoid high may represent buoyant upper mantle trapped between continental cratons, causing isostatic uplift. Vectors show the load applied to the North America craton. (b) Extra gravitational potential energy (GPE) associated with the Yellowstone hotspot (circle). We calculate the GPE gradient for geoid above 5 m, filtered to remove wavelengths shorter than 700 km (corresponding to signal generated from density structure above ~100 km) and longer than 4000 km (to eliminate signal from the lower mantle). Geoid-based western U.S. GPE is centered over Yellowstone, which differs from the GPE estimated from crustal structure (see Fig. A3). This suggests that Yellowstone GPE is due to density structure deeper than our assumed 125 km depth of compensation. (c) Basal tractions from the global-flow model of *Becker and O'Connell* [2001], and root drag. Horizontal tractions are shown with vectors and vertical tractions are contoured in km, representing dynamic topography. Also shown is where *Grand*'s [1997] S-wave velocity is >2% fast when averaged between 175-250 km depth. We use this to represent the area of deepest cratonic root. To this root we apply NE- and NW- oriented loads to represent drive or drag interaction with the craton.

Figure A5. Weighting functions. (a) Relation between horizontal principal stresses and tectonic regime. Regime is given a vaue with the relation $0.5+0.5\ atan(p/d)/atan(3)$ for $p=(\sigma_1+\sigma_2)/2$ and $d=(\sigma_1-\sigma_2)/2$, where σ_1 and σ_2 are maximum and minimum horizontal principal stresses, respectively. This measure of regime is essentially that of *Simpson* [1997], only rescaled. Compression is positive, and 3D pressure (average normal stress) is the reference zero value [*Simpson*, 1997; *Flesch et al.*, 2000]. (b) Misfit as a function of difference between observed and predicted orientation angle and regime. Contour level is 0.1. For each site, goodness of angle and regime are $Ga=exp[-(Pa-Sa)/(Da\ \sqrt{2})]$ and $Gr=exp[-(Pr-Sr)/(Dr\ \sqrt{2})]$, respectively, for predicted and observed angles Pa and Sa, predicted and observed regimes Pr and Sr. Da and Dr are the standard deviations in the Ga and Gr values, respectively. Site misfit is given by $M=1-(Ga\cdot Gr)/2+(Ga+Gr)/4$, and total model misfit is the sum of site misfits.

Figure A6. Model results. Results shown use the gravitational potential energy estimate with the 1250 km cross

over wavelength (Fig. A3), although all three best-fit models are nearly the same. (a) Comparison of observed and modeled stress. (b) Modeled loads and stress. Red and blue bars show modeled horizontal principal deviatoric stresses, with red indicating tension and blue compression relative to pressure (i.e., vertical deviatoric stress equals the sum of the two horizontal stresses shown, but of the opposite sign). Loads in TN/m except root drag, which is in units of MPa acting over the area of the root (Fig. A4c). Error estimates, shown with bars at vector head or tail, are discussed in the text. Vectors and error bars shown in red have been diminished in magnitude by a factor of three. (c) Misfit between modeled and observed stresses at each site, calculated using relations given in Fig. A5.

Figure A7. Covariance matrices. (a) Model misfit second derivative matrix evaluated about best solution (where first derivatives are zero) and normalized so that diagonal values are one. Black dots in lower matrix triangle indicate negative values (matrix is symmetrical). Note that cross-variance values tend to be small, indicating little tradeoff between most parameters. (b) Eigenvectors of (a). Black dots represent negative values. Note that most eigenvectors are dominated by a single value, indicating that most parameters are resolvable.

Tables

Table A1. Stress values used in modeling.

Lon	Lat	Style EofN	SHmax	Location	Ref
143.0	66.0	.32	33	central Siberia	1
165.7	60.9	.36	123	north Kamchatka	
181.9	63.8	.65	107	NW Bering Sea	1
195.0	65.5	.81	95	Seward Peninsula	1,2
204.0	66.0	.54	-60	west Alaska	1
211.6	65.2	.44	156	central Alaska	1
211.8	70.5	.52	148	north Alaska	1
220.0	61.5	.32	-5	Yakutat, SW Alaska	1,2,3
224.4	66.5	.39	35	NW Yukon	3
228.0	64.8	.16	28	NE Yukon	3
235.0	62.5	.12	41	SW of Great Bear Lake	3
240.0	60.0	.16	49	W of Great Slave Lake	
243.0	55.0	.15	43	Canada Great Plains	
238.0	53.2	.22	11	S British Columbia	1
241.0	52.2	.17	40	SE British Columbia	
258.3	78.0	.41	63	Queen Elizabeth Is	1
265.6	67.1	.35	55	NW of Hudson Bay	1
224.5	56.3	.34	26	Alexander Islands	1
227.2	53.2	.29	23	Queen Charlotte Is.	1,4
234.0	50.0	.43	28	north Vancouver Is.	
236.5	48.3	.22	-15	Juan de Fuca Straight	5
238.0	48.0	.34	2	Seattle	
240.0	47.0	.26	-9	Columbia Basin, WA	
249.5	44.7	.86	-40	Yellowstone	
245.9	44.1	.89	-42	central Idaho	
247.3	41.1	.88	0	Salt Lake City	
247.5	39.3	.89	22	eastern Great Basin	
245.0	38.0	.79	39	southern Great Basin	
243.5	39.3	.88	27	central Great Basin	
240.0	42.0	.65	2	NW Great Basin	
242.2	40.5	.68	28	north-central Nevada	
241.4	38.8	.59	27	Walker Lane, Nevada	
236.5	45.0	.33	3	northwest Oregon	
236.3	39.5	.52	22	NW California	6
238.6	37.6	.39	30	Berkeley California	
240.2	35.5	.22	31	west-central CA	
242.0	34.4	.35	7	Los Angeles	
252.5	40.0	.83	-52	Colorado Rocky Mtns	
255.0	40.0	.82	-27	Colorado Great Plains	
263.0	40.0	.26	-87	KA-NB-CO	
256.0	36.5	.88	104	west CO-NM	
253.0	35.0	.89	5	Rio Grande Rift, NM	
251.0	31.0	.87	9	Juarez, Mexico	
249.8	26.1	.61	18	Gulf of California	
274.0	17.3	.53	21	west of Belize	
268.8	16.4	.51	43	Mexican Isthmus	
261.0	19.2	.88	81	south of Mexico City	
260.0	20.0	.92	80	Mexico City	

257.3	19.1	.75	43	Colema, Mexico	
258.5	27.5	.52	179	Monterrey, Mexico	
265.4	32.5	.40	59	Texas-Arkansas	
263.0	35.0	.48	74	Oklahoma	
269.9	35.5	.40	75	New Madrid	
275.0	32.0	.12	61	western Georgia	
275.0	36.0	.27	83	west Tennessee	
270.0	42.0	.26	52	near Chicago	
277.8	39.5	.25	75	NE Ohio	
282.0	42.4	.24	71	Lake Erie	
285.0	40.5	.17	68	eastern Pennsylvania	7
287.0	39.0	.25	61	east of New Jersey	
282.0	38.0	.09	-79	Delaware	
292.5	40.5	.24	93	SE of Boston	
300.0	43.0	.22	44	east of Nova Scotia	
290.0	48.0	.18	64	St Lawrence Inlet	
300.0	33.0	.25	78	SE of Bermuda	
284.4	20.7	.38	35	east Cuba	1
292.0	26.0	.30	63	NW of Puerto Rico	
299.4	21.4	.39	-60	NE of Puerto Rico	
302.0	18.5	.50	-9	near Antilles	
305.0	20.0	.27	-9	east of Antilles	

Data from the World Stress Map Project shown in Fig. 2 [*Reinecker et al*., 2004] are used in all stress estimates. Additional data included in stress estimation are from sources indicated in the right column.

1. http://www.seismology.harvard.edu/CMTsearch.html
2. *Paige et al*. [1991].
3. *Mazzotti and Hyndman* [2002]; *Hyndman et al*. [2005].
4. *Bird et al*. [1995].
5. *Wang et al*. [1995]; *Lewis et al*. [2003].
6. *Provost and Houston* [2003].
7. *Seeber et al*. [1998].

Table A2. Reference ocean ridge.

Depth	0	2.5	8.5	9.5	11.0	12.5	14.5	16.5	19.0	23.0	28.0	38.0
Temp.	0	200	450	550	650	750	850	950	1050	1150	1250	1350
Density	1030	2800	3320	3309	3297	3286	3275	3264	3252	3241	3230	3218

Depth in km to top of layer, temperature in C^{o}, density in kg/m^{3}.

Table A3. Model misfit.

	Root			NoRoot		
Xover	misfit	B&O	<|S|>|	misfit	B&O	<|S|>
600	**11.1590**	**19%**	**1.25**	13.3226	5%	1.12
1250	**11.3429**	**20%**	**1.13**	12.6684	12%	1.01
2500	**11.6033**	**20%**	**1.05**	12.8931	24%	0.97
4000	12.6224	47%	1.30	13.8028	33%	1.11
5000	12.9443	42%	1.37	13.1861	18%	1.24
7500	13.4701	45%	1.51	13.8203	40%	1.45

Table A4.

GPE Xover (km)	600	1250	2500
Siberia TN/m	2.46	3.09	2.64
Kam -/	-1.77	-1.47	-2.14
Kam //	-0.73	-0.70	-0.07
AlSub//	0.64	0.55	1.01
AlSub W	1.49	1.46	0.99
AlSub M	-3.12	-2.86	-2.69
AlSub E	0.32	0.44	1.37
Yakutat	6.00	6.00	6.00
Q.C. -/	3.31	3.00	1.59
Q.C. //	3.50	2.54	2.54
Q.C. S.	3.90	2.51	2.75
Cas //	2.24	2.49	2.26
Cas -/	2.67	2.00	1.48
CasS -/	-4.15	-4.03	-3.53
SAF -/	1.02	0.87	0.71
SAF //	2.09	1.62	1.29
Baja //	1.08	0.66	0.96
Baja -/	-1.62	-0.96	-0.40
Mex N.	2.13	1.40	1.20
Mex S.	-1.10	-0.97	-2.05
Car //	2.12	1.90	1.69
Car -/	1.50	1.60	2.10
PR sub	-4.31	-3.60	-3.62
So. Am.	2.74	2.58	3.49
N Atl %	100	100	100
Yell PE %	45	26	3
Base Dr %	19	20	20
Root NW MPa	0.96	-0.27	0.94
Root NE MPa	5.02	4.60	4.09

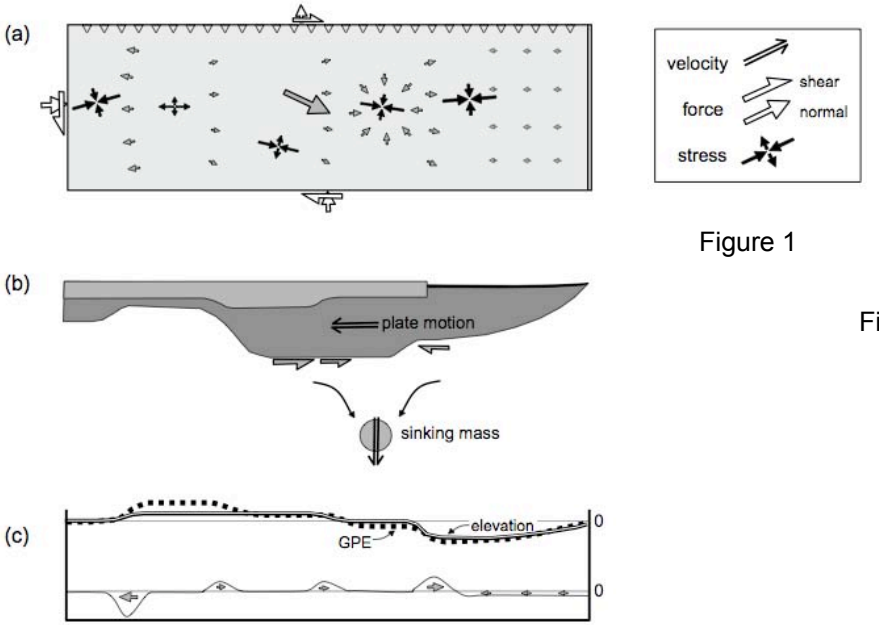

Figure 1

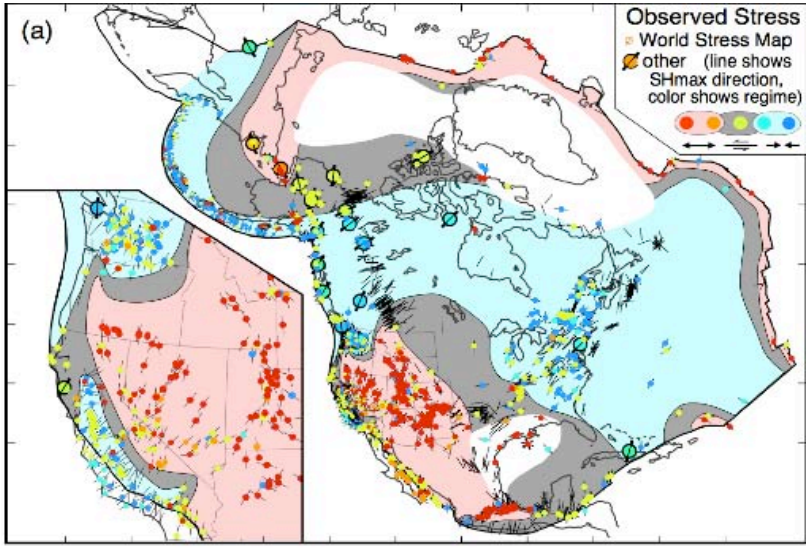

Figure 2

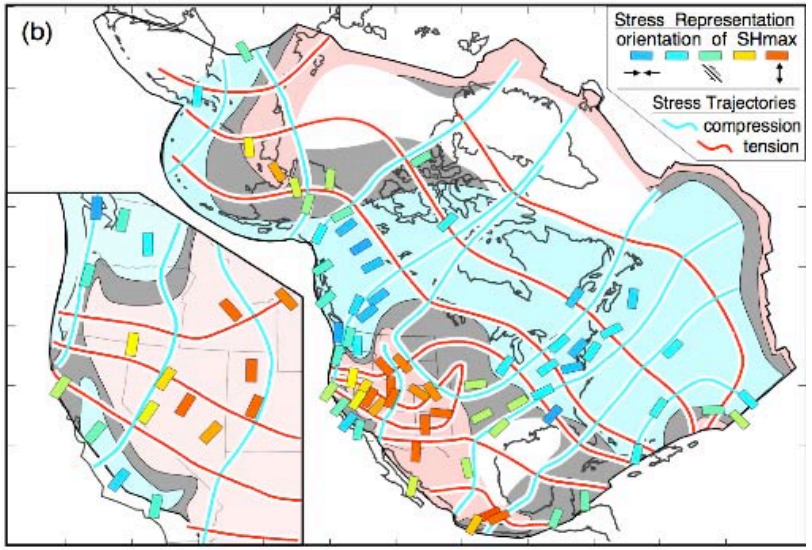

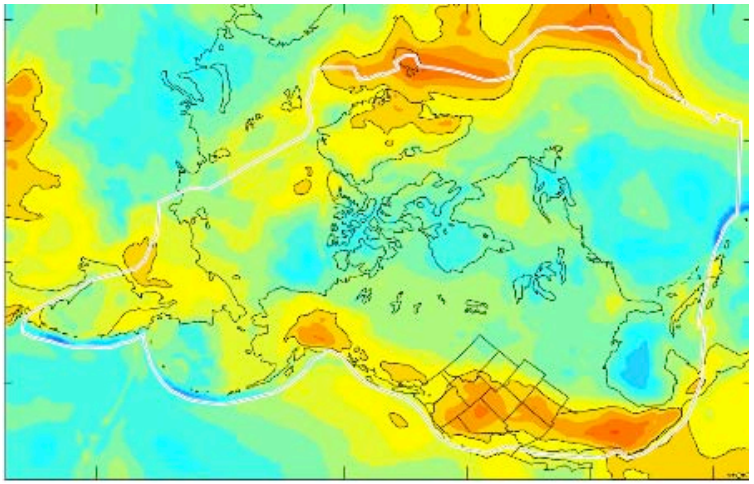

Figure 4

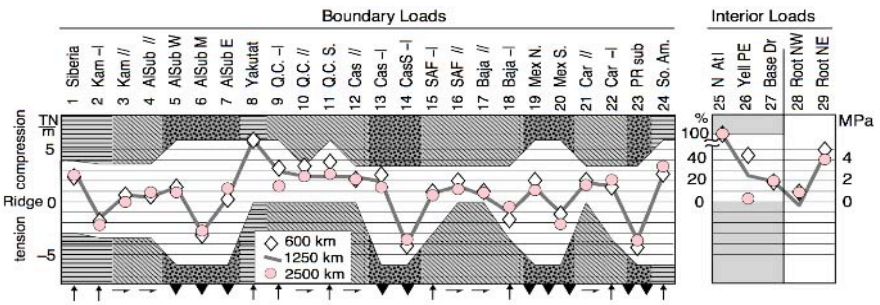

Figure 3

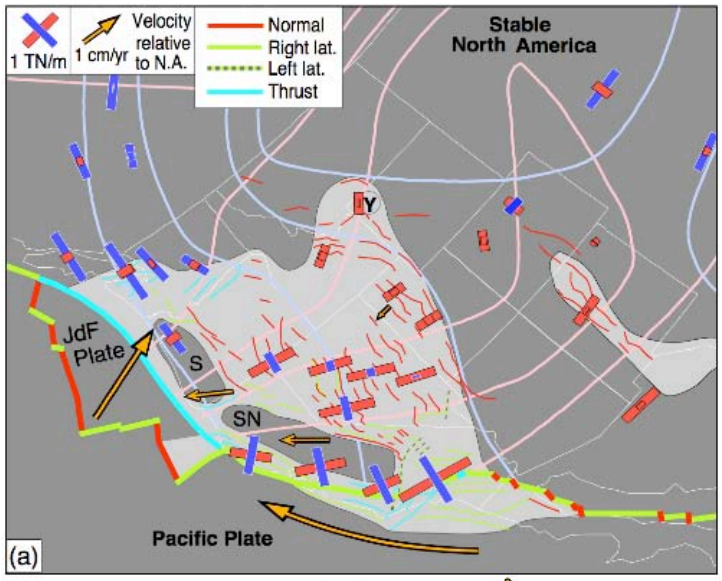

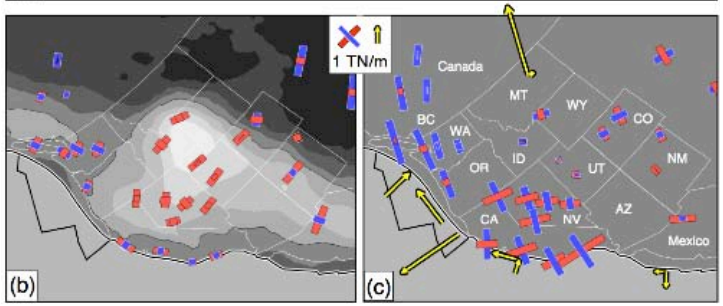

Figure 6

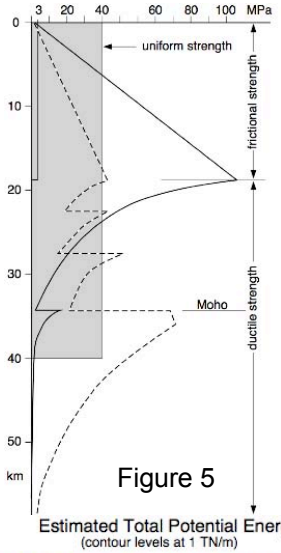

Figure 5

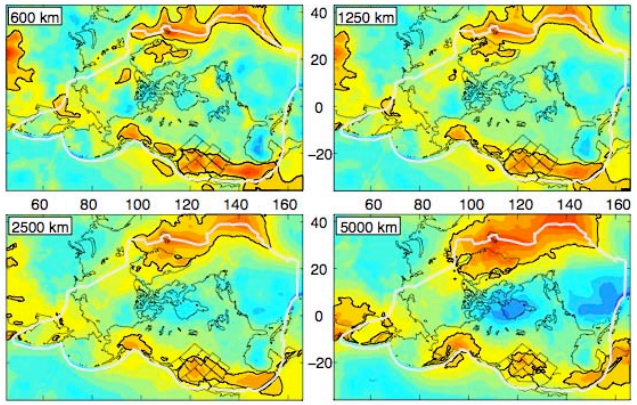

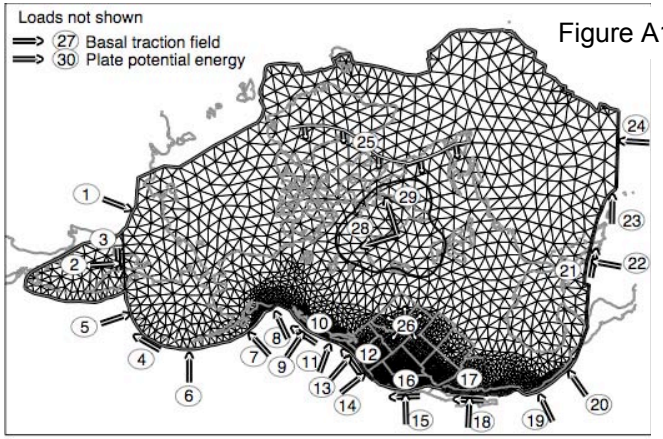

Figure A1

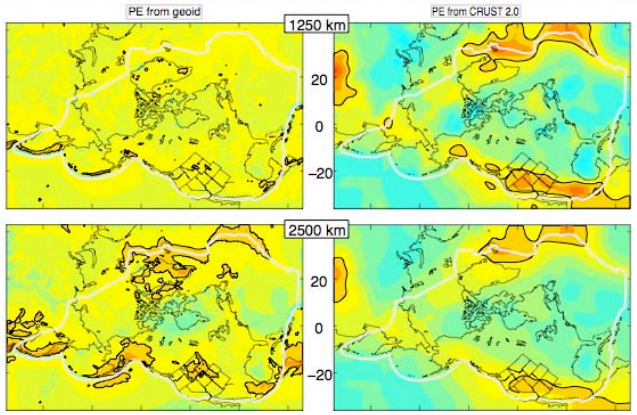

Figure A3

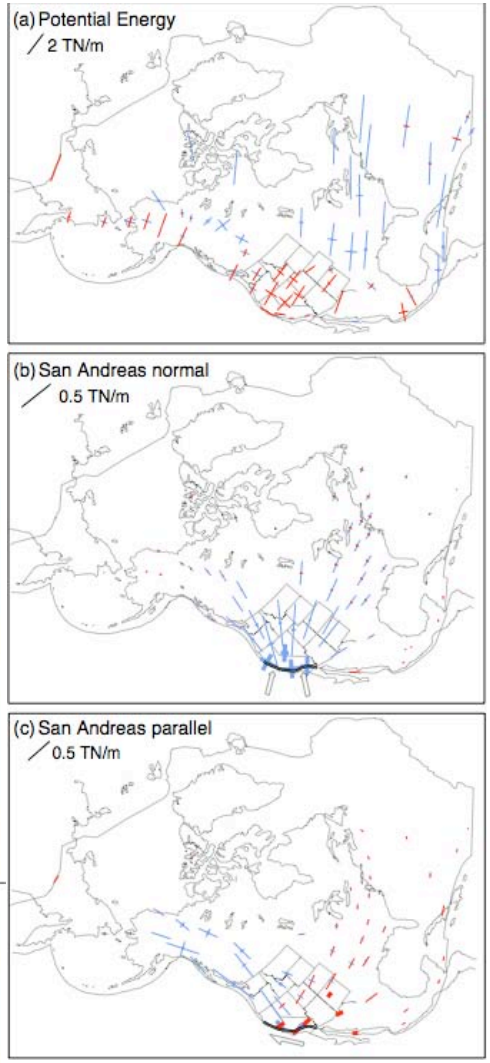

Figure A2

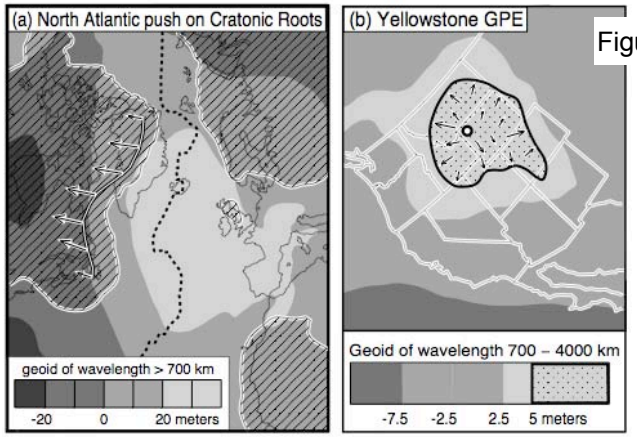

Figure A4

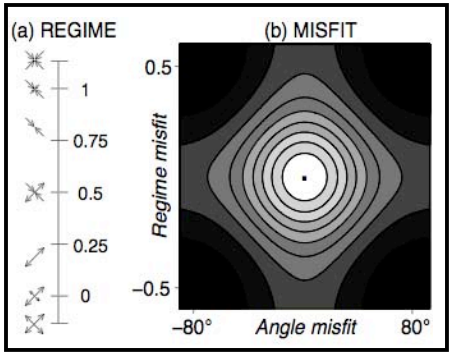

Figure A5

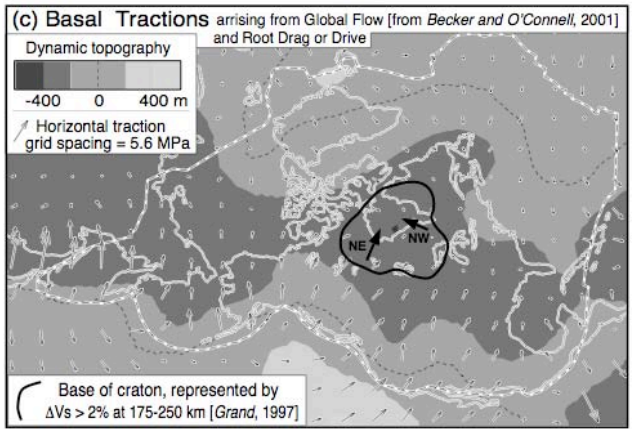

Figure A6

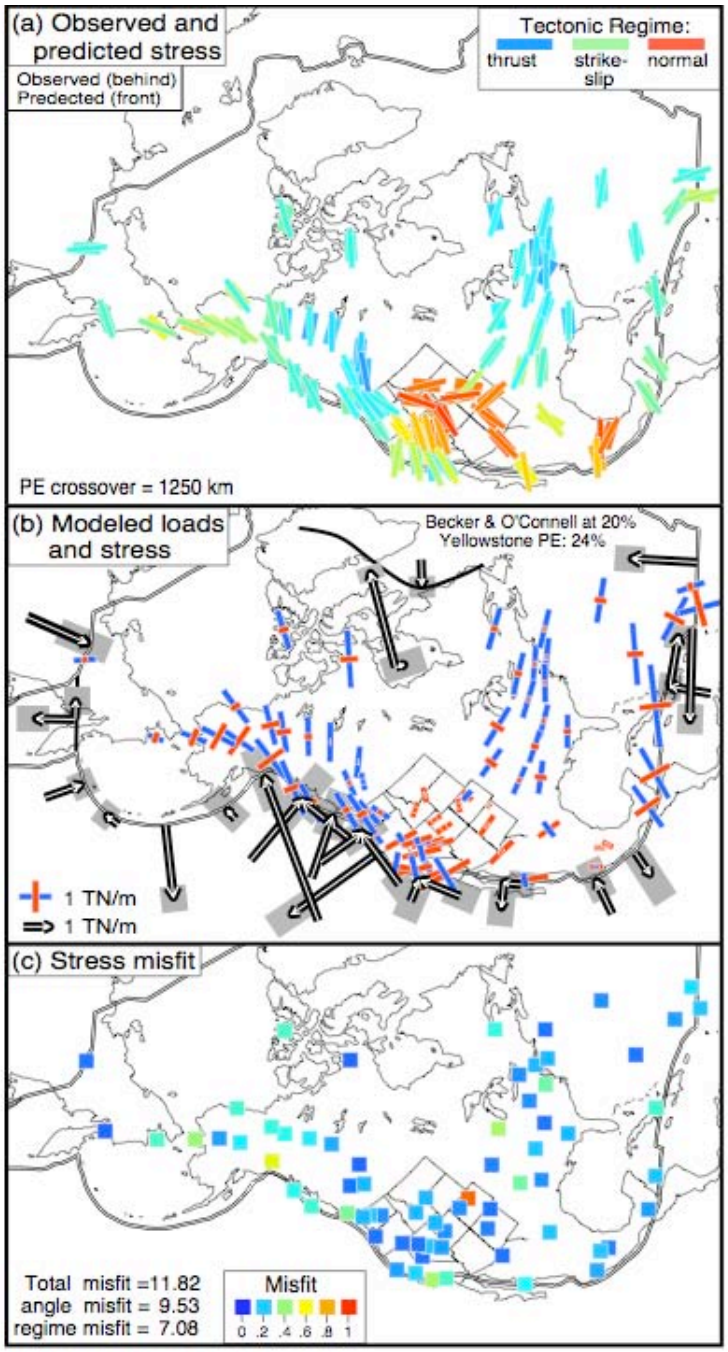

Figure A7